MASTER

Epitaxial graphene, is it really graphene?
a combined STM/HREELS study of graphene on silicon carbide

van de Ruit, K.

Award date:
2007

Epitaxial Graphene, is it really Graphene? A combined STM/HREELS study of graphene on Silicon Carbide

Kevin van de Ruit

December 5, 2007

Abstract

Graphene, a single layer of graphite, is a zero band gap semiconductor material characterized by its linear band structure, which opens up interesting new possibilities as an electronic material. Graphene can be grown on top of silicon carbide (SiC) using a heating process in which the silicon evaporates and the carbon is left behind forming a graphene layer. Electronic structure information of the formed graphene layer, obtained with Scanning Tunneling Spectroscopy (STS), shows that the local electron density of states is highly spatially dependent. High Resolution Electron Energy Loss Spectroscopy (HREELS) measurements reveal that the phonon band structure of the grown graphene film is comparable to the calculated structure for a single layer of free standing graphene, indicating a small chemical interaction with the substrate.

Contents

Chapter 1

Introduction

Graphene, a single layer of graphite, has recently (since 2004) attracted much attention of the physics community. This might seem strange, since its trademark, a linear band structure, has been known since 1947 [1] and its relevance to fundamental physics has been known since 1982 [2]. Even more so, since measurements from 1990 on epitaxial layers of graphene on TaC(100) seem to already show the linear dispersion of graphene [3][1]. However, it took a full fourteen years since these discoveries before the findings of Geim [4] shocked the world by showing that single free standing layers of graphene can also be obtained from graphite using Scotch tape. The real difference between the discovery of Geim compared to the epitaxial layers obtained in the 90's is that Geim was able to make the link to the fundamental physics involved in graphene.

This illustrates the importance of the fundamental physics of graphene. Such important physics largely stems from the many "symmetries of graphene", which are:

- The two carbon atoms in the unit cell are symmetric by a point symmetry operation.
- Electrons and holes have the same dispersion relation.
- The linear dispersion relation is found at two points in the Brillouin zone, K and K'. These two points are symmetric.
- Electron spin symmetry is not broken.

Not only do these symmetries hold in graphene, they hold for a large energy range (approx 1eV), which makes graphene a nearly ideal system. The behavior of the electrons in this system are closely related to the physics of massless Dirac fermions [5]

Such characteristics give rise to many (new) physical phenomena, such as [5]

- The Klein paradox, which describes the tunneling of massless Dirac fermions trough high barriers. Such tunneling is characterized by the remarkable fact that the tunneling probability does not decay with the barrier width and height.

[1] This is a review paper. The paper discussing TaC(100) in more detail is unfortunately only available in Japanese, which might already explain why this did not lead to a direct break trough.

- The Anomalous quantum Hall effect, which differs from the conventional quantum Hall effect by the observation of a Landau level at the Fermi energy, related to a Berry's phase of π for electrons in graphene as opposed to a Berry's phase of 2π for conventional semiconductors [6].
- The ability of graphene to conduct a supercurrent (Josephson effect) [7].
- The possibility of superconductivity in pure or doped graphene [8, 9].
- The possibility of a negative refractive index lens (a Veselago lens) for electrons in graphene [10].
- Spin valves for electrons in graphene [11].
- Spin valves based on the symmetry between the K and K' point in the brilloun zone [12].

Many of these phenomena still exist strictly in theory, such as the possibility of superconductivity and the possibility of manufacturing a Veselago lens. This is an effect of the enormous amount of theoretical work done since Geim's discovery in 2004. So far experimental work has not been able to check many of these theories. For such experimental work it is of crucial importance to obtain graphene layers, maintaining the characteristic properties of graphene. A possible way of obtaining such layers is epitaxial growth on top of a single crystal. Silicon Carbide(SiC) is an ideal candidate for such a single crystal. Not only has SiC already attracted much attention by itself by enabling a high power, high temperature semiconductor devices, making it a well studied and available material, it also has the advantage that it is able to form epitaxial graphene from carbon which is already present in the material itself. The only thing required in order to form the layers on top of SiC is a heat treatment.

Shortly after Geim's publication, De Heer [13] revealed the first prove of graphene formed on SiC. However many properties of the epitaxial graphene layers remain to be checked, such as the linear band structure and the electron-hole symmetry. In other words:

Epitaxial Graphene, is it really Graphene?

In order to answer this question, epitaxial layers have been grown on SiC and have been characterized, as discussed in chapter 3. STM measurement and HREELS measurements have been conducted to reveal the local electronic structure and phonon properties, as discussed in chapter 4. Firstly, the general theory on graphene, SiC and the used measurement techniques is addressed in chapter 2.

Chapter 2

Theory

In this chapter the theory necessary for understanding the measurements is presented. Firstly, the basic properties of graphene and silicon carbide will be discussed. Then the used experimental techniques will be discussed.

2.1 Graphene

In this section the basic properties of graphene will be discussed, starting with its crystal structure, followed by its electronic structure and finally the phonon dispersion of graphene.

2.1.1 Crystal Structure

Graphene is known to posses a hexagonal crystal structure, shown in figure 2.1a. From this crystal structure the unit cell can be obtained, showing that there are two carbon atoms in the unit cell, simply named A and B. The unit vectors a_1 and a_2 can be written:

$$a_1 = \frac{a}{2}(3, \sqrt{3}, 0)$$
$$a_2 = \frac{a}{2}(3, -\sqrt{3}, 0),$$

with $a = 1.418$Å the nearest neighbor distance. These unit vectors then result in reciprocal lattice vectors:

$$b_1 = \frac{2\pi}{3a}(1, \sqrt{3}, 0)$$
$$b_2 = \frac{2\pi}{3a}(1, -\sqrt{3}, 0), .$$

With these the First Brillouin Zone (FBZ) can be determined as shown in figure 2.1b. The corners of the FBZ are denoted K and K'. Notice that the three K' point are identical under translation of one of the reciprocal lattice vectors.

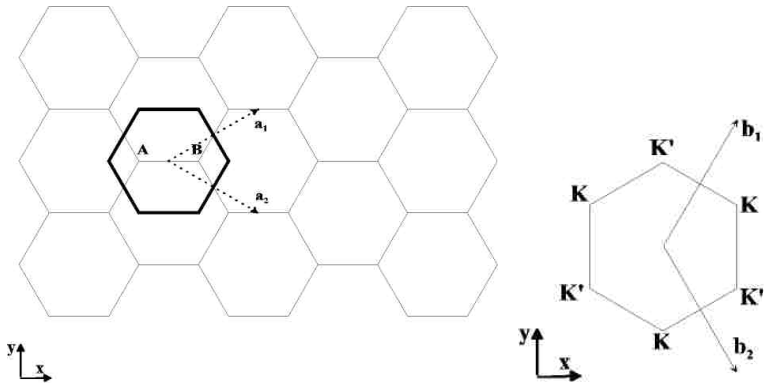

(a) **(b)**

Figure 2.1: *a) Graphene crystal structure. The thick lines indicate the Wigner-Seitz unit cell, containing two carbon atoms named A and B. Dotted arrows indicate the unit vectors, a_1 and a_2. b) First Brillouin Zone (FBZ) of graphene, along with the reciprocal lattice vectors, b_1 and b_2. The two distinct corners of the FBZ are denoted K and K'. Notice that all K' points are the same under translation by the reciprocal lattice vector.*

2.1.2 Electronic structure

In this section a tight binding approximation of the π electron band in graphene is made in analogy of Wallace [1], but formulated closely to Peres *et al* [14]. Carbon is the sixth element in the periodic table and has an electronic configuration of $1s^2 2s^2 2p^2$. The $1s$ electrons are core electrons (almost 300eV below E_F) and will not be taken into account. The $2s$ and $2p$ electrons are best represented in an sp_2 configuration, which is a linear combination of s and p orbitals in such a way that the three hybrid σ orbitals lie in the same plane each under an angle of 60° and one π orbital perpendicular to this plane. For each atom the σ bonds are then chosen in the direction of their nearest neighbor, resulting in a bonding (anti-bonding) band with a maximum (minimum) still $>$ 4eV below (above) E_F depending on the substrate. This is still not very relevant for the physics we want to study. For this we will only take into account the π-orbitals.

For these orbitals a thight binding hamiltonian can be formulated:

$$H = -t \sum_{<i,j>,\sigma} (a^\dagger_{i,\sigma} b_{j,\sigma} + b^\dagger_{j,\sigma} a_{i,\sigma}), \tag{2.1}$$

where $a^\dagger_{i,\sigma}$ ($a_{i,\sigma}$) creates (annihilates) an electron on an A-site at R^A_i, $b^\dagger_{j,\sigma}$, ($b_{j,\sigma}$) creates (annihilates) an electron on an B-site at R^B_j, $< i, j >$ denote all combinations with R^A_i and R^B_j nearest neighbors and $t \approx 2.7eV$ denotes the hopping energy.

This Hamiltonian can be solved using the fourier transformation of $a^\dagger_{i,\sigma}$,$a_{i,\sigma}$,$b^\dagger_{i,\sigma}$ and $b_{i,\sigma}$,

shown here only for $a^\dagger_{i,\sigma}$ together with its inverse transformation

$$a^\dagger_{k,\sigma} = \frac{1}{\sqrt{N}} \sum_i \exp[-ikR^A_i] a^\dagger_{i,\sigma},$$
$$a^\dagger_{i,\sigma} = \frac{1}{\sqrt{N}} \sum_k \exp[ikR^A_i] a^\dagger_{k,\sigma}.$$

Now using the following vectors

$$\delta_1 = \frac{a}{2}(-1, \sqrt{3}, 0),$$
$$\delta_2 = \frac{a}{2}(-1, -\sqrt{3}, 0),$$
$$\delta_3 = a(1, 0, 0),$$

which point from any A-site to its three neighbours, the Hamiltonian can be rewritten as:

$$\begin{aligned}
H \quad &= -t \sum_{<i,j>,\sigma} \Big(\quad \frac{1}{\sqrt{N}} \sum_k \exp[ikR^A_i] a^\dagger_{k,\sigma} \frac{1}{\sqrt{N}} \sum_{k'} \exp[-ik'R^B_j] b_{k',\sigma} \\
&\qquad + \frac{1}{\sqrt{N}} \sum_k \exp[ikR^B_j] b^\dagger_{k,\sigma} \frac{1}{\sqrt{N}} \sum_{k'} \exp[-ik'R^A_i] a_{k',\sigma} \Big) \\
&= -\tfrac{t}{N} \sum_{i,l\in\{1,2,3\},\sigma} \Big(\quad \sum_{k'} \exp[ik'R^A_i] a^\dagger_{k',\sigma} \sum_k \exp[-ik(R^A_i + \delta_l)] b_{k,\sigma} \\
&\qquad + \sum_k \exp[ik(R^A_i + \delta_l)] b^\dagger_{k,\sigma} \sum_{k'} \exp[-ik'R^A_i] a_{k',\sigma} \Big) \\
&= -\tfrac{t}{N} \sum_{k,l\in\{1,2,3\},\sigma} \Big(\quad \exp[ik\delta_l] a^\dagger_{k',\sigma} b_{k,\sigma} \sum_{k'} \sum_i \exp[i(k'-k)R^A_i] \\
&\qquad + \exp[ik\delta_l] b^\dagger_{k,\sigma} a_{k',\sigma} \sum_{k'} \sum_i \exp[i(k-k')(R^A_i)] \Big) \\
&= \sum_{k,\sigma} \Big(\phi(k) a^\dagger_{k',\sigma} b_{k,\sigma} \quad + \phi^*(k) b^\dagger_{k,\sigma} a_{k',\sigma} \Big) \\
&= \sum_{k,\sigma} [a^\dagger_{k,\sigma}, b^\dagger_{k,\sigma}] \quad \begin{bmatrix} 0 & \phi(k) \\ \phi^*(k) & 0 \end{bmatrix} \begin{bmatrix} a_{k,\sigma} \\ b_{k,\sigma} \end{bmatrix}
\end{aligned} \tag{2.2}$$

with

$$\phi(k) = -t \sum_{l=1}^{3} \exp[ik\delta_l].$$

Solving the Eigenvalues for the matrix in equation 2.2 gives $E = \pm|\phi(k)|$. Since each atom donates one electron to the π-band the Fermi-level in this model is located exactly at $E = 0$. With some basic math, the zeros of $\phi(k)$ can be found to be at the corners of

the FBZ:

$$K = \frac{2\pi}{3a}(1, \frac{1}{3}\sqrt{3}, 0),$$
$$K' = \frac{2\pi}{3a}(1, -\frac{1}{3}\sqrt{3}, 0).$$

A Taylor approximation around $k = K$ gives:

$$|\phi(K + k)| = 0 + \frac{3}{2}at|k| + O(k^2). \tag{2.3}$$

this linear part corresponds to the typical Dirac cones shown in figure 2.2.

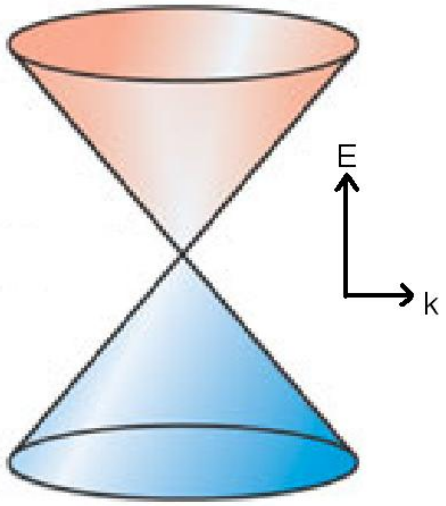

Figure 2.2: *Schematic drawing of the Dirac cones, which represent the linear band structure of graphene.*

2.1.3 Phonons

Theoretical calculations for the phonon dispersion of free standing graphene yield results that are nearly indistinguishable to those for graphite [35]. These calculations compare well to measurements of the phonon modes of graphite [46]. To illustrate the phonon modes, the measured phonon dispersion for an epitaxial bilayer of graphene, which is very similar to the phonon dispersion of graphite/free standing graphene, is shown in figure 2.3. The phonon dispersion shows three acoustical branches: ZA, LA and TA and three optical branches, ZO, LO, and TO. This number of branches is consistent with a unit cell consisting of 2 atoms. The phonon dispersion measured in the $\Gamma - M$ direction and the $\Gamma - K$ direction seem very similar.

The transverse phonon in the direction perpendicular to the graphene layer, the ZA and ZO branch, seem to be lower in energy than the in plane phonon branches LA, TA and

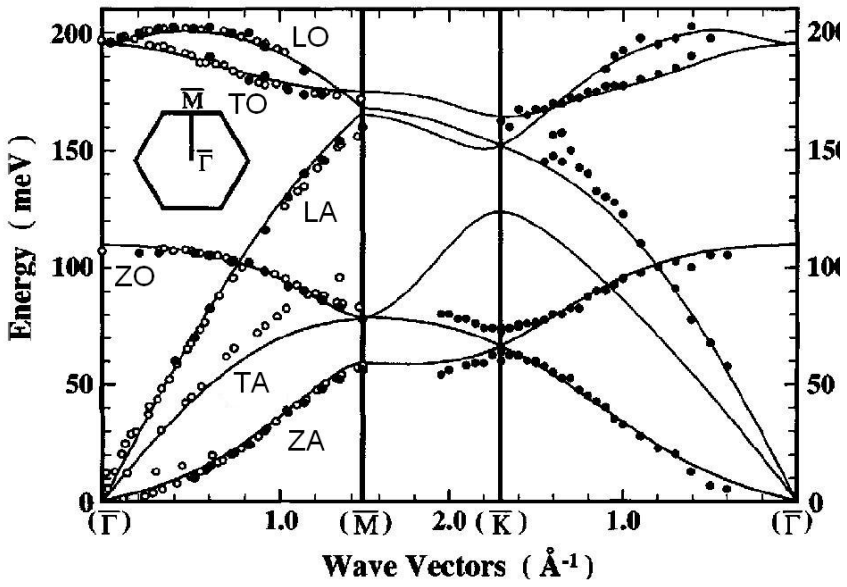

Figure 2.3: *Measured phonon dispersion for bilayer graphene[19] on $BC_3/NbB_2(0001)$ using HREELS(solid circles) compared to ab initio calculation(solid lines) and measurements on graphite(open circles).*

LO, TO respectively. This shows that the carbon atoms in the graphene layer are more weakly bound in the z-direction than they are in the in plane directions. These conclusion can be made using a bond force model such as presented in [47]. This model also provides information on the interaction between the substrate and graphene for epitaxial graphene layers. Which is why the phonon modes of graphene on SiC have been determined using HREELS as discussed in section 4.2.

2.2 Silicon Carbide

For a studying the interaction between SiC and graphene a basic knowledge of SiC is useful. Therefore the crystal structure and electronic properties will be discussed in this section.

Silicon carbide is a material which occurs in many different crystal structures. All of them consist of hexagonally packed layers stacked in different ways. On top of a hexagonal packed layer as shown in figure 2.4, a next layer can position itself either on a B-site or a C-site(stacking on an A-site would not be closed packed, and is not observed for SiC). Since both these sites are still rotationally symmetric we choose the B-sides by convention. On top of this second layer however there is no symmetry between A-sites and C-sites. Different stacking thus result in different crystal structures. An ABCABC...-stacking sequence turns out to be a fcc crystal structure, the structure for β-SiC also known as 3C-SiC. For SiC, ABAB...-stacking is known as 2H-SiC, ABCBABCB...-stacking is known as 4H-SiC, ABCACBABCACB...-stacking is known as 6H-SiC.

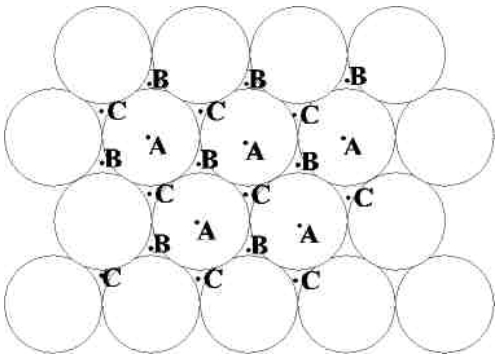

Figure 2.4: *An illustration of possible stacking positions.*

For epitaxial growth of graphene 4H-SiC and 6H-SiC are the most popular forms of SiC. Lattice constants for these materials are $a = (3.07 \pm 0.01)\mathring{A}$ for both 4H-SiC and 6H-SiC and $c = 4 \times 2.51$Å and $c = 6 \times 2.51$Å for 4H-SiC and 6H-SiC respectively [16].

SiC is an indirect wide bandgap semiconductor with $E_g = 3.29$eV and $E_g = 3.10$eV for 4H-SiC and 6H-SiC respectively. Bandstructures are shown in figure 2.5.

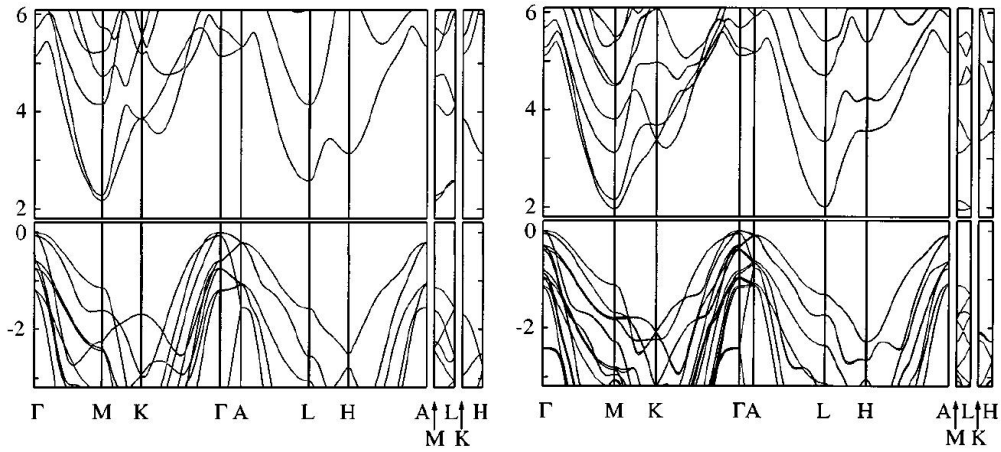

Figure 2.5: *Calculated band structures for a) 4H-SiC and b) 6H-SiC [16].*

2.3 Experimental techniques

The different measurement techniques used in this thesis are discussed in this chapter. Firstly, LEED will be discussed using the explanation from [61], followed by an explanation of STM from [62]. And finally HREELS will be explained, also from [61].

2.3.1 Low Energy Electron Diffraction

Low energy electron diffraction (LEED) is employed to determine the surface structure of single crystals and its ordered adsorbate layer [54, 59]. The technique is based on the diffraction of low energetic electrons directed towards the surface. A monochromatic low energy electron beam (50 200 eV) is directed onto a surface. Electrons are back scattered elastically and show constructive interference related to the structure of the impinged surface. The mean free path of the electrons in a solid is very small generally not more than a few atomic layers making this a very surface sensitive technique [54].

Electrons can be described as an electromagnetic wave with the wavelength given by the De Broglie relation:

$$\lambda = \frac{h}{\sqrt{2m_e E_{kin}}}, \tag{2.4}$$

in which:

λ	wavelength of the electrons
h	Plancks constant
m_e	rest mass of an electron
E_{kin}	kinetic energy of the electron

The electrons arrive at the surface at normal incidence and interference occurs according to the Braggs equation:

$$\sin\alpha = \frac{n\lambda}{a} = \frac{nh}{a\sqrt{2m_e E_{kin}}}, \tag{2.5}$$

in which:

α	angle between scattered electrons and the surface normal
n	order of diffraction (an integer)
a	distance between scatterers, i.e. the lattice constant for clean surface

Figure 2.6 shows schematically a LEED setup. Often LaB6 is used as filament for the electron gun to provide the primary electron beam. A hemispherical fluorescent screen with its focus on the sample collects the backscattered electrons. In front of this screen two to four grids are positioned to ensure a field-free region between the sample and the analyzer and to filter the secondary (inelastically scattered) electrons. On the fluorescent screen the diffracted electrons are made visible as a pattern of spots.

As the relationship between interatomic distances and the diffraction pattern is inverse (eq. 2.5), the diffraction pattern shows a reciprocal lattice, i.e. larger distances between the LEED spots corresponds to small interatomic distances and vice versa. The construction of the reciprocal lattice is straightforward. From a surface lattice characterized by two base vectors a1 and a2, the reciprocal lattice follows from:

$$a_i \cdot a_j^* = \delta_{ij}, \tag{2.6}$$

in which:

a_i	the base vectors of the real lattice (i= 1, 2)
a_j^*	the base vectors of the reciprocal lattice (j= 1, 2)
δ_{ij}	Kronecker delta

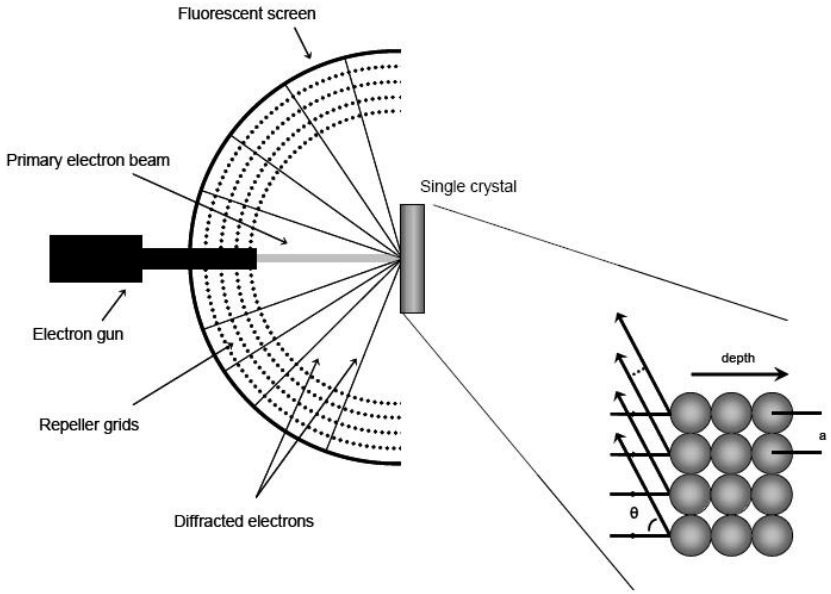

Figure 2.6: *Schematic representation of a low energy electron diffraction setup. A beam of monoenergetic electrons scatters elastically from a surface. Back scattered electrons show constructive interference related to the structure of the impinged surface. Directions of the constructive interference are made visible on a fluorescent screen.*

This means that a_1 is perpendicular to a_2^* and a_2 is perpendicular to a_1^* and that there is an inverse relationship between the lengths of a_1 (a_2) and a_1^* (a_2^*).

The base vectors should reflect the unit cell of a given lattice. In other words, the vectors should construct the smallest parallelogram from which the lattice can be constructed through translations only. To a first approximation, the LEED pattern for a surface with an order adlayer consists simply of the superposition of the reciprocal lattice of the adlayer on the reciprocal lattice of the substrate surface.

Often, the periodicity of ordered structures from adlayers is simply a multiple of the substrate lattice vectors (a commensurate adlayer). In this case, the Woods notation [60] can be used, where the structure is expressed with respect to that of the substrate metal. Figure 2.7 shows two simple but often occurring examples including the actual LEED pattern. In these cases, the unit cell of the adlayer can be determined quite easily with LEED. The positions of the adsorbates with respect to the surface (i.e. which binding site) are not directly obvious. Performing LEED quantitatively, where the intensities of the various diffracted beams are recorded as a function of the incident electron beam energy to generate so-called I-V curves, may provide accurate information on atomic positions [54, 59]. To interpret these I-V curves, they need to be compared with simulated curves, based on a rigorous theoretical description, where not only the diffraction by the topmost layer need to be calculated, but also multiple scattering, inelastic and quasi-elastic scattering need to be implemented. Addressing this theory is beyond the scope of the thesis [54, 59].

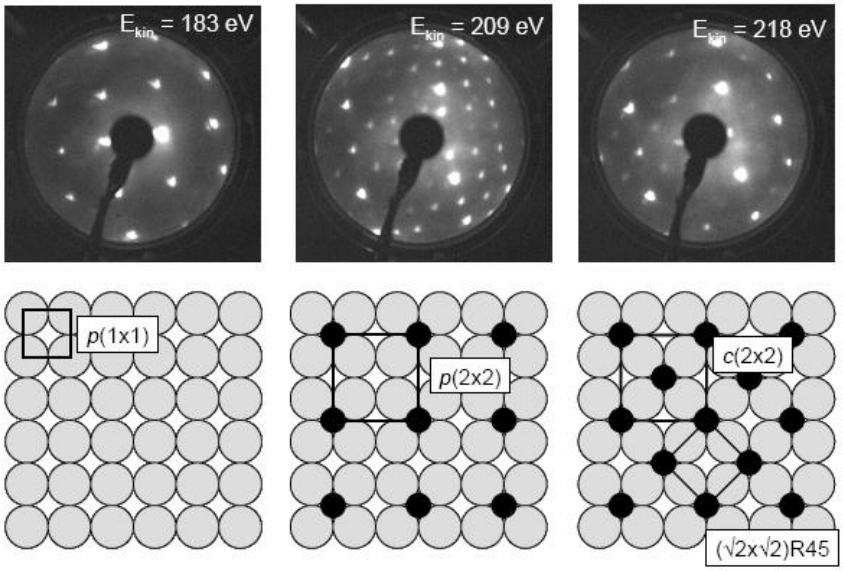

Figure 2.7: *LEED images of a clean Rh(100) (left) and after adsorption of 0.25 ML of oxygen (middle) and 0.50 ML of oxygen (right) with below their corresponding real-space structure models. Note that in the LEED images the middle spot is missing because it falls directly on the electron gun.*

2.3.2 Scanning Tunneling Microscopy

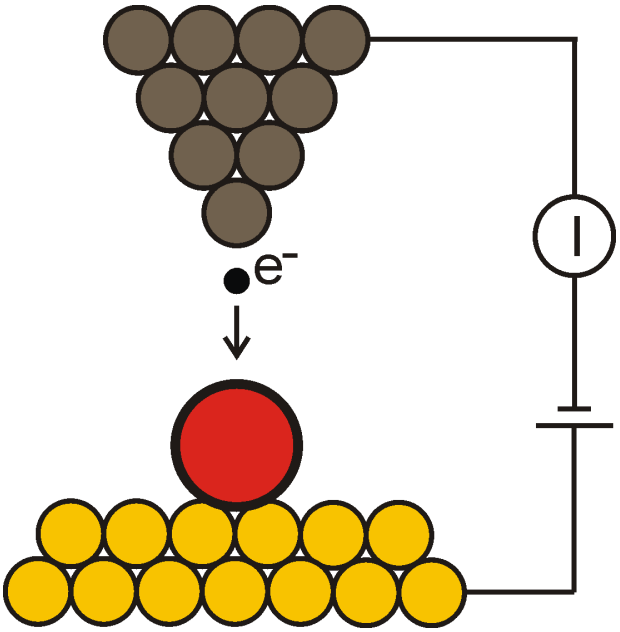

Figure 2.8: *The standard setup of an STM schematically drawn.*

A scanning tunneling microscope (STM) is a microscope which can produce images of surfaces with atomic resolution utilizing tunneling currents. It is invented in 1981 by Gerd Binnig and Heinrich Rohrer of IBM's Zurich Lab in Switzerland [50], which earned them the Nobel Prize in Physics in 1986. The standard setup is shown in figure 2.8. An atomically sharp tip is brought to within a few atomic diameters of the surface under investigation. There is no physical contact, so there is a very small overlap of the wavefunctions of the surface with the wavefunctions of the end atom of the tip. When a bias voltage, ranging from 1 mV to 10 V, is applied between the sample and the tip, electrons tunnel across this gap with a probability that increases exponentially as the tip approaches the sample. The tunneling current is roughly given by the following equation [51],

$$I = cV \exp\left[-d\sqrt{\Phi}\right] \tag{2.7}$$

where c is a constant, Φ is the barrier height of the tunneling gap, measured in electron volts, V is the applied voltage and d is the distance between tip and surface, measured in Angstroms. This exponential dependence makes the STM extremely sensitive to detect small changes in the surface height due to individual atoms. Scanning over a surface and measuring - at fixed bias - the tunneling current at each point gives in principal a topographic map of the surface under investigation. In practice, a feedback loop corrects the vertical position of the tip to maintain a constant current, called the setpoint current, and records the vertical corrections as the *topographic mapping* and the deviations from the setpoint current as the *current mapping*.

Equation 2.7 is however an approximation that is valid only in the *wide band limit*, which assumes a constant density of states of both sample and tip. How the density of states of the sample and tip come into play, is shown in figure 2.9.

This figure shows the energy level diagram for the system consisting of the sample, the tip and the vacuum in between. Figure 2.9a shows the case where the sample and tip are independent, so their vacuum levels are considered to be equal. Their respective Fermi energies (E_F) lie below the vacuum level by their respective work functions ϕ_s and ϕ_t. If the sample and tip are in thermodynamical equilibrium, their Fermi energies must be equal, as is shown in figure 2.9b. Electrons attempting to pass from sample to tip encounter a potential barrier, which they can tunnel through if the barrier is sufficiently narrow. When a voltage V is applied to the sample, its energy levels will be shifted upward (if $V < 0$) or downward (if $V > 0$) in energy by the amount $|eV|$, where e is the electronic charge. At positive sample bias, the net tunneling current arises from electrons that tunnel from the occupied states of the tip into the unoccupied states of the sample, as is shown in figure 2.9c. At negative sample bias, the net tunneling current arises from electrons that tunnel from the occupied states of the sample into the unoccupied states of the tip, as is shown in figure 2.9d. An expression for this tunneling current can be found using the WKB method [52], and is given in equation 2.8,

$$I = \int_0^{eV} \rho_s(E)\rho_t(E - eV)T(E, eV)dE \tag{2.8}$$

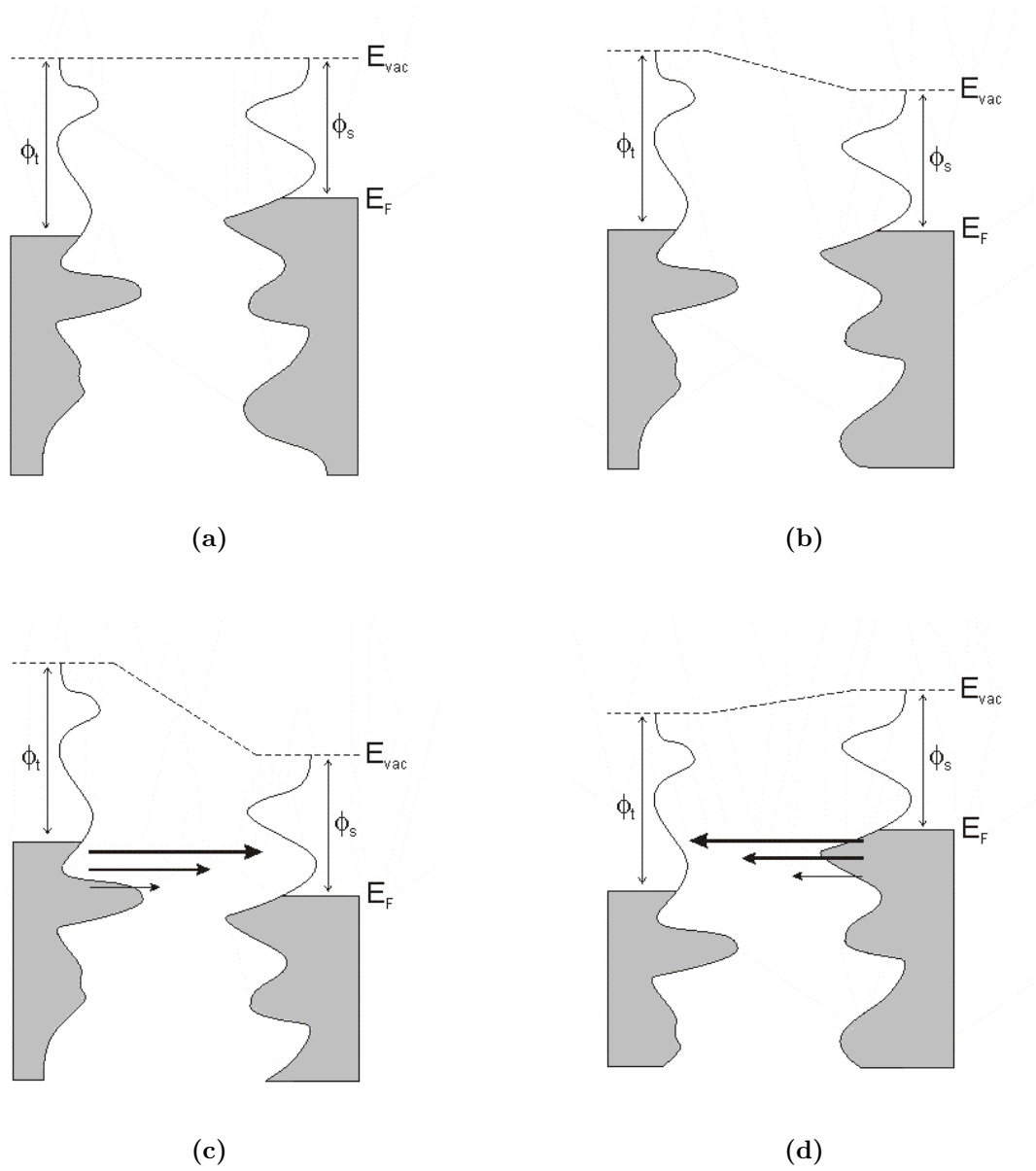

Figure 2.9: *Energy level diagrams for sample and tip. a) Independent sample and tip. b) Sample and tip at thermodynamical equilibrium. c) Positive sample bias. Electrons tunnel from tip to sample. d) Negative sample bias. Electrons tunnel from sample into tip.*

where $\rho_s(E)$ is the (local) density of states of the sample, $\rho_t(E)$ is the density of states of the tip and $T(E, eV)$ is the transmission probability. In the WKB approximation, this probability is given by the following equation [52],

$$T(E, eV) = \exp\left[-\frac{2Z\sqrt{2m}}{\hbar}\sqrt{\frac{\phi_s + \phi_t}{2} + \frac{eV}{2} - E}\right] \tag{2.9}$$

where m is the electron mass, $\hbar$ is Planck's constant, Z is the tip-sample separation and E is the energy measured with respect to the Fermi level. This expression again shows the exponential dependence on the tip-sample separation, but also the influence of E. States with the highest energy have the longest decay lengths into the vacuum, so most of the tunneling current arises from electrons lying near the Fermi level of the negative-biased electrode. The dependence of the tunneling current on the overlap of wavefunctions of tip and sample (equation 2.8) implies that STM does not reveal the positions of atoms themselves, but rather the electronic density of states, which is assumed to be higher around the atoms. It also implies that with an STM, it is possible to obtain spectroscopic information with atomic spatial resolution.

2.3.3 HREELS

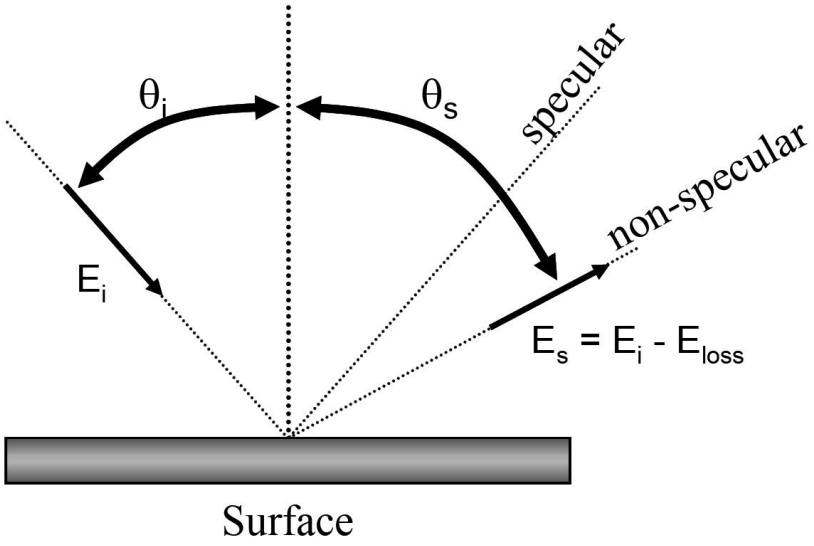

Figure 2.10: *Schematic of the electron scattering geometry in HREELS.*

In (high resolution) electron energy loss spectroscopy (HREELS) a monoenergetic beam of slow electrons (1200eV) is focused onto the surface of a single crystal (figure 2.10). Electrons with an energy in the range of a few electron volts sample only a few atomic layers [54]. As they approach or exit the crystal, they interact with the vibrational modes

of the single crystal surface. The energy spectrum of electrons reflected from the surface thus contains information about excited vibrations according to the equation:

$$E = E_0 - h\nu \tag{2.10}$$

in which

E	energy of the scattered electron
E_0	energy of the incident electrons
h	Plancks constant
ν	frequency of the excited vibration

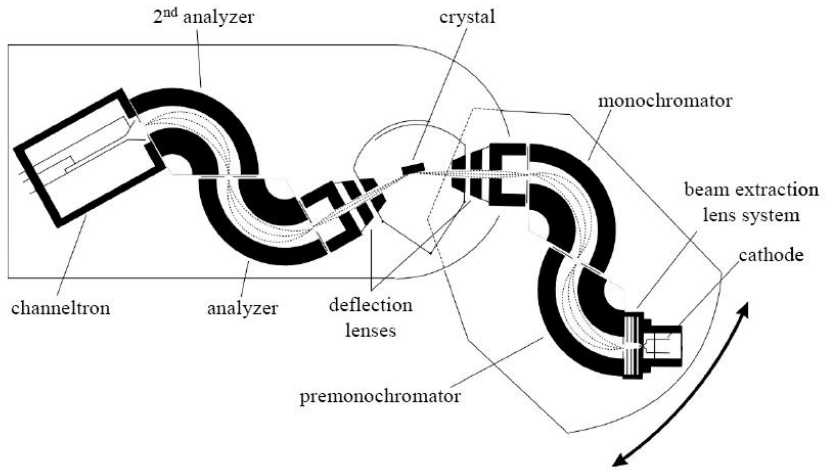

Figure 2.11: *Schematic representation of an Ibach type EEL spectrometer. The monochromator side can rotate with respect to the analyzer side.*

The vibrational modes of molecules adsorbed on the surface provide direct information on the nature of the chemical bonds between the molecule and the substrate.

Figure shows a schematic view of the spectrometer used (Ibach-type [38]). For a detailed description about the operation of the EELS we refer to Refs. [38, 55]. A LaB_6 cathode emits electrons which are focused on the entrance slit of the monochromator. Modern EEL spectrometers use two monochromators. Both are 127° cylindrical deflectors on which a potential-difference can be realized over the top and bottom plate and over the inner and outer cylindrical walls to discriminate between energies (or velocity) of the incoming electrons. Only the electrons with the right kinetic energy, the so-called pass energy move through the monochromators. The acquired monoenergetic beam is focused onto the sample by a set of deflecting lenses. To prevent disturbing electric fields the sample is magnetically shielded from the surroundings. The scattered electron beam is then focused on the entrance slit of the dual analyzer. The analyzers are identical to the monochromators. The intensity of the electron beam is in the order of tens of pA, therefore a channeltron is used to amplify the signal. To allow both specular and off-specular operation of the spectrometer, the monochromator side can be rotated to vary the angle of incidence of the electron beam on the crystal.

High resolutions (< 10 meV) can only be acquired when low kinetic energies of the electrons are used. These electrons sense work-function differences due to various metallic materials in the spectrometer. To circumvent this, all parts of the spectrometer have to be coated with a uniform conducting layer which does not oxidize, such as gold or graphite. Further, the whole spectrometer is placed in a double μ-metal box to shield it from external magnetic fields. The power supply has to be extremely stable. Noise and ripple superimposed on the desired voltages would seriously limit the resolution. Maybe the major consequence of using electrons is the necessity of performing the experiments in ultrahigh vacuum (UHV).

Electron scattering mechanisms

Different electron scattering mechanisms to excite surface vibrations play a role. The (surface) dipole scattering contributes by far the most to the loss spectrum in the mainly used specular mode, i.e. where the angle of incidence equals the angle of backscattering with respect to the surface normal (see Fig. 2.10). The (electron) impact scattering is much more dominant in an off-specular operated experiment. The mechanisms will be briefly explained and the corresponding selection rules will be discussed.

Surface dipole scattering

Surface dipole scattering is a long-range effect mediated by the Coulomb field whereby an incoming charged electron is influenced by a vibrating dipole at the surface. The incident electrons do not actually hit the surface, the excitation is caused at larger distances, a value of 60 A has been calculated by Ibach and Mills [38]. Dipole scattering can be treated (semi-) classically [56, 57], or quantum-mechanically [58]. However, both approaches show little significant differences. The incident electron and its image produce an electric field. This electric field interacts with dipoles on the surface. As the electric field vector is normal to the surface, only vibrations which have a non-zero dipole moment perpendicular to the surface are excited [54]. With group theory it can be shown that this requirement can be translated into the condition that only vibrations which belong to the totally symmetric representations (A_1, A' and A) can be observed in dipole scattering [38]. The parallel momentum is conserved, but due to the large momentum of electron, the shift in angle is small for dipole scattering. Hence, the intensity distribution is sharply peaked in the specular direction, $\theta_s = \theta_i$.

The theoretical description of dipole scattering lead to three observations:

1. There is strong pronounced forward scattering. In other words, the intensity distribution is strongly peaked in specular direction.

2. Only vibrations with a dynamic dipole moment normal to the surface contribute to the loss spectrum; particularly for molecules close above the metal surface.

3. The scattering intensity is related to the dynamic dipole moment.

Impact scattering

Impact scattering is a short range scattering process from the ion core. The scattering is much more isotropic, hence not in the specular direction, but over wide range of angles in and out of the plane of incidence. As the HREELS generally accept electrons from a very limited angle, the intensity of the impact scattered electrons is very low. By changing the scatter angle peaks from the different scatter mechanisms can be distinguished. Moreover, the cross section of impact scattering increases with increasing impact energy, whereas the cross section of dipole scattering is inversely proportional to the impact energy. This ability to discriminate between the two scatter mechanisms provides important information about the binding geometry of a species. This mechanism can excite modes with a non-normal dipole. In most cases, all modes can, in principle, be observed away from the specular direction. However, selection rules are not entirely absent in impact scattering [38]. In addition, by impact scattering an electron can also take an amount of energy from excited molecules and, hence, leave the surface with a higher energy. This results in a negative loss, i.e. a peak on the negative axis of the EEL spectrum.

Chapter 3

Sample preparation and characterization

The reason silicon carbide was selected as the platform for growing graphene is for its unique properties. SiC has been extensively studied in the past and is used commonly as wide band gap semiconductor in electronic applications. Moreover, under certain high temperature and high vacuum conditions, Si evaporates from SiC surface and the remaining carbon forms naturally graphene films on its surface. Therefore, it is obvious that a large atomically flat SiC surface is necessitous before growing graphene films on its surface. Single crystal SiC substrates with a SiC(0001) surface have been commercially obtained. However, their surface has been full of scratches (see figure 3.1b), which required an additional polishing step (hydrogen etching) to obtain atomically flat surface. Resulting flat SiC substrates have been heated to produce a graphene layer on them and consequently analyzed by AFM, STM and HREELS.

3.1 Samples

Three different types of SiC samples have been used with two different SiC polytypes (4H-SiC and 6H-SiC):

Samples A,B,C,D 4H-SiC samples with sizes of 5×5 mm with a polished $< 0.5°$ off-axis SiC(0001) surface, obtained from University Wafer[1].

Samples E,F 4H-SiC samples with sizes of 12×5 mm with a polished $4°$ off-axis SiC(0001) surface, production grade, obtained from SiCrystal AG[2]

Sample G A 13×4 mm 6H-SiC sample obtained from Horn [17], with a specially treated SiC(0001) surface

[1] See http://universitywafer.com
[2] See http://www.sicrystalag.com

The samples obtained from the suppliers showed typically 2 nm deep scratches on their surfaces as shown in figure 3.1a. Therefore, these samples have been prepared by an etching step, which will be discussed in the next section. The 6H-SiC sample obtained from Horn [17] did not need an additional hydrogen etching step because it had already a specially treated SiC(0001) surface, which showed large atomically flat regions in AFM (figure 3.1b). Two step edges are observed on the same AFM image with atomically high SiC step edges (0.5 nm).

The most important difference between the samples obtained from the two different suppliers is the difference in off-axis polishing angle. Having a higher off-axis polishing angle results in a higher density of step edges.

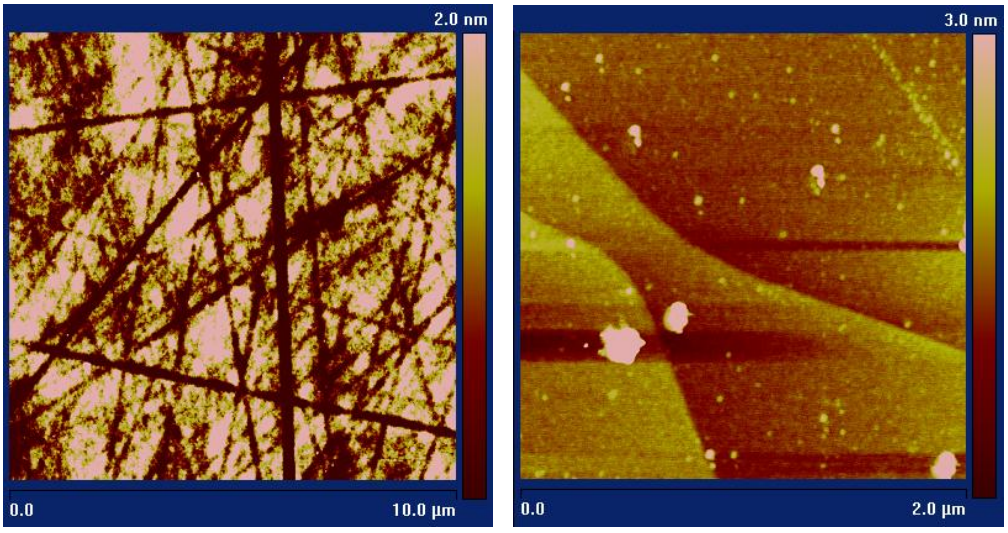

(a) **(b)**

Figure 3.1: *a) AFM image of a typical polished sample as obtained from the supplier. b) AFM image of sample G.*

3.2 Hydrogen Etching

As already mentioned, samples obtained from the suppliers showed scratches on the surfaces, while atomically flat regions are required. Therefore, an etching step has been used to go from samples with a scratched surface similar to that shown in figure 3.1a to a surface with large atomically flat regions, such as shown in figure 3.1b.

Etching SiC surfaces to obtain atomically flat regions has been described in [15], showing that etching at 1600°C for 15 min in a hydrogen flow should result in large atomically flat areas on the surface. However, the etching temperatures, duration and amount of hydrogen flowing over the sample are parameters which might depend on the setup, and experiments have to be performed to obtain the correct parameters.

The etching experiments were performed by Phillips using an etching facility at the High Tech Campus[3]. Their facility can reach temperatures of over 1700°C at which they are able to flow pre-heated highly pure (less than 1ppm water or oxygen) hydrogen gas over the substrates. Temperature ramping is very slow (ramp up 15°C/min, ramp down 30°C/min).

3.2.1 Results

Four experiments have been performed, as shown in table 3.1. Etching results from different treatments have been studied using an optical microscope and AFM, as shown in figures 3.2 and 3.3. In this section these measurements will be discussed.

Table 3.1: *Overview of performed etching experiments, all were conducted at* 1600°C.

Exp no #	Hydrogen flow	Duration	Sample(s) produced
1	200ml/min	30min	A
2	450ml/min	15min	B
3	450ml/min	90min	C,E,F
4	450ml/min	120min	D

Experiment 1 has resulted in a sample, which shows large deep pits on the surface, as it can be seen in the microscopic image of sample A shown in figure 3.2a. A study of the surface using AFM points out that the surface is very rough in most places, and an atomically flat region was found rarely, as shown in figure 3.3a. Therefore, this sample was not used in further experiments.

Experiment 2 has resulted in a sample with smaller features in its microscope image compared to experiment 1, as shown in figure 3.2b. The AFM images obtained on sample B depict that no large atomically flat areas are obtained, and the surface quality has not been improved with this etching treatment.

Experiment 3 has resulted in samples with only small etching pits, as depicted for sample C in figure 3.2c and sample E in figure 3.2d. Sample E showed an additional roughness compared to sample C, which is possibly related to the higher off-axis cut off this sample ($< 0.5°$ for samples A,D and $\approx 4°$ for samples E,F). AFM analysis of samples C and E unveil similar results, where sample C shows large atomically flat terraces (figure 3.2c), while on sample E, atomically flat terraces with a reduced size are formed (figure 3.3d). This is also consistent with a larger off-axis polishing angle. The observed step edges are aligned, which is accordance with the observation that step edges prefer to align to the $< 1100 >$ set of directions [15]. However, the terraces contains some "crack-like" features, which were not observed by Ramachandran [15].

The samples produced in experiment 4 were similar to those produced in experiment 3.

[3]Philips Research/High Tech Campus 4/room 1.410/mailstop 12/5656 AE EINDHOVEN/The Netherlands

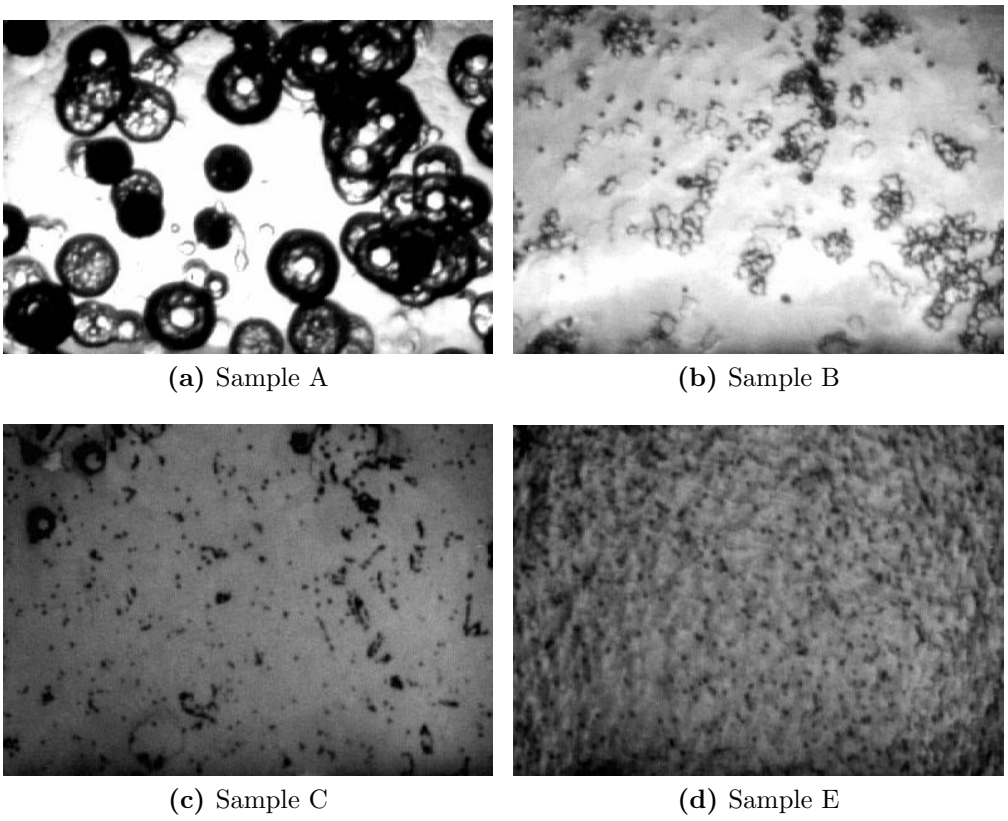

(a) Sample A **(b)** Sample B

(c) Sample C **(d)** Sample E

Figure 3.2: *a) Optical microscopic image (620x420 μm) of sample surfaces after etching treatments.*

3.2.2 Conclusions

Etching for 90 or 120 minutes at 1600°C using a hydrogen flow of 450ml/min successfully produces samples with micrometer large atomically flat areas.

Shorter etching periods resulted in samples, which do not show (many) atomically flat areas. Possibly, the etching procedure has not been fully completed.

The terraces contain some "crack-like" features and the optical microscopic images still show small etching pits, so optimalization of the parameters is still needed.

The samples with higher off-axis polishing, samples E and F, appear to have a higher density of step edges and higher roughness.

3.3 Heat treatment

In order to form a graphene layer on top of a SiC substrate, a heat treatment is needed to thermally decompose Si from the SiC surface, the remaining carbon forms then spontaneously a graphene layers. The aim was to reproduce the procedure reported by De Heer et al. [13]. De Heer et al. applied successively heat treatments and determined the surface

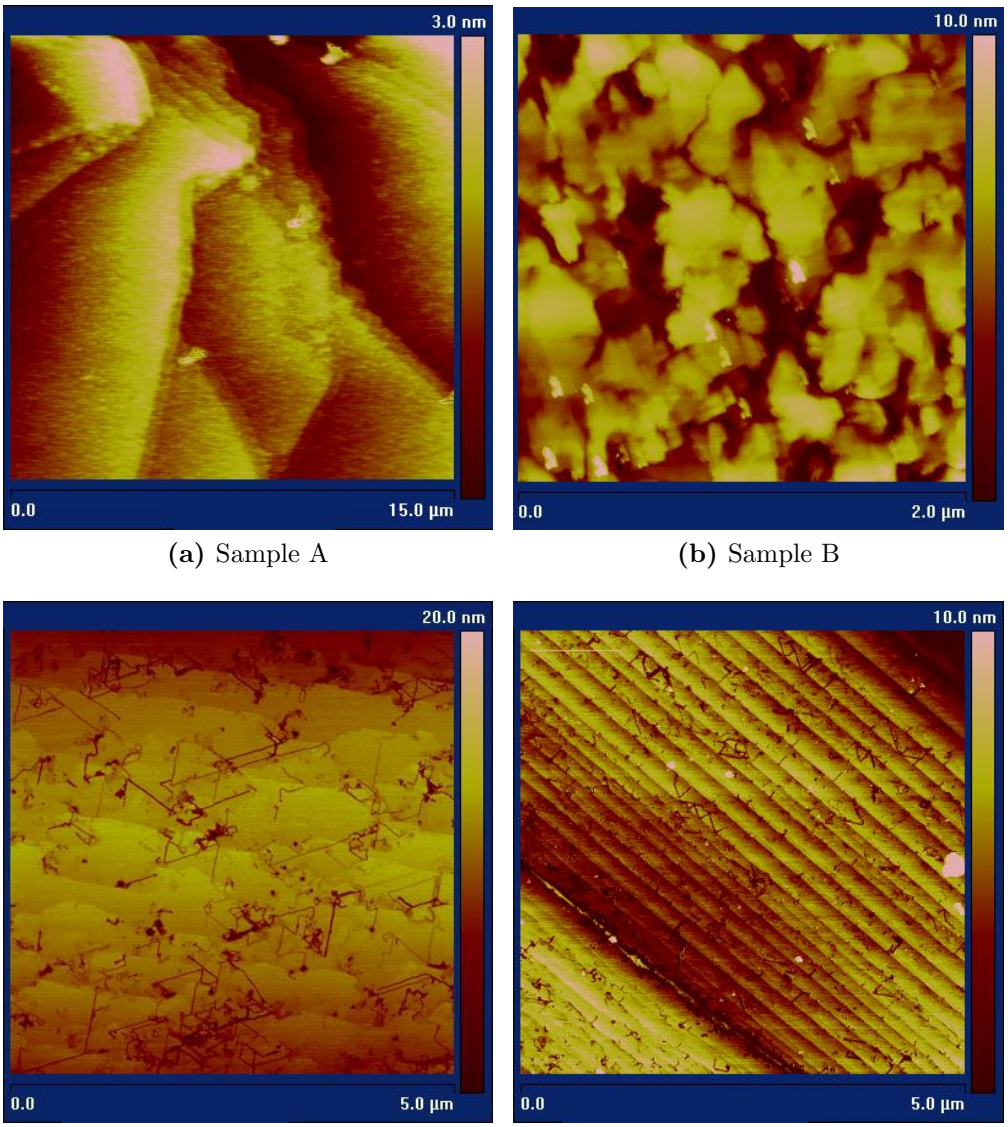

(a) Sample A **(b)** Sample B

(c) Sample C **(d)** Sample E

Figure 3.3: *AFM images of samples prepared in etching experiments 1 a), 2 b), and 3 for sample C c) and sample E d).*

reconstruction using LEED. The heat treatments and the surface structure determined by LEED measurements will be discussed in this section followed by STM measurements in the next section.

Different heat treatment processes of SiC are described in the literature. A table containing information on the reconstructions formed using different heat treatments are shown in table 3.2.

A difficulty in comparing the different treatments already starts with the fact that all of the authors other than De Heer [13] use annealing in a Si-flux. This means that the

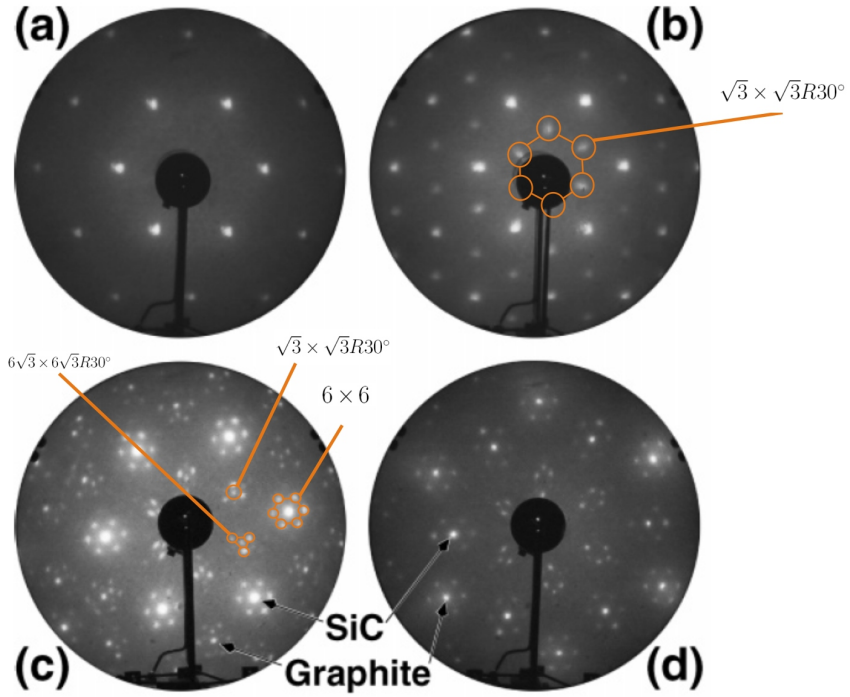

Figure 3.4: *Heating results from De Heer et al. [13]. a) LEED at* 177eV *after* 10 *minutes at* 1050°C. *Oxide is removed and LEED shows the SiC* 1×1 *pattern. b) LEED at* 171eV *after an additional* 3 *minutes at* 1100°C. *Showing a* $\sqrt{3} \times \sqrt{3}R30°$. *AES shows much less than a monolayer(ML) of carbon. c) LEED at* 109eV *after an additional* 20 *minutes at* 1250°C. *Showing a "*$6\sqrt{3} \times 6\sqrt{3}R30°$*" reconstruction, a graphite* 1×1 *pattern as well as* 6×6 *spots around the graphite* 1×1 *and SiC* 1×1 *spots. AES shows approximately 1 ML of carbon. d) LEED at* 98eV *after an additional* 8 *minutes at* 1400°C. *Showing a similar pattern as in d). AES shows approximately 2.5 ML of carbon.*

oxide on the SiC sample is removed using a bombardment of Silicon atoms, typically by keeping a Silicon sample at melting point close to the SiC sample. In De Heer [13] it is reported that heating to 1050°C is also sufficient to remove oxide from the sample.

Despite of the differences in the method of removing the oxide, it is nevertheless remarkable that the measurements in De Heer [13] still show a $\sqrt{3} \times \sqrt{3}R30°$ pattern up to temperatures as high as 1250°C, while in all other papers this is not described.

It is also remarkable that Chen et al. [25] reported that a $6\sqrt{3} \times 6\sqrt{3}R30°$ pattern is obtained after a heat treatment at 1050°C, while Forbeaux et al. [21] reported that a $6\sqrt{3} \times 6\sqrt{3}R30°$ pattern only starts showing up after heating to 1150°C. This could mean that the temperature measurements reported in literature are not very accurate.

3.3.1 Experimental setup for the heat treatment

For the heat treatment a home-build e-beam heater with a special sample plate were used, as shown in figure 3.3.1. The sample plate is thinner at certain places to prevent large

Table 3.2: *Overview of performed heating experiments together with observed LEED patterns from literature*

De Heer [13]	Forbeaux [21]	Chen [25]	Starke [22]	Rollings [30]
6H-SiC	6H-SiC	6H-SiC	4H-SiC	6H-SiC
	900°C, si-flux 3×3	850°C, si-flux, $2-3$min. 3×3	800°C,low si-flux, 30min. 3×3	850°C, si-flux, $20-30$min. 3×3
		950°C,5min. $\sqrt{3} \times \sqrt{3}R30°$	980°C $\sqrt{3} \times \sqrt{3}R30°$	1000°C,5min. 1×1
1050°C, 10min. 1×1	1050°C, few min. $\sqrt{3} \times \sqrt{3}R30°$	1050°C, 5min. $6\sqrt{3} \times 6\sqrt{3}R30°$ $\sqrt{3} \times \sqrt{3}R30°$		
1100°C, 3min. $\sqrt{3} \times \sqrt{3}R30°$	1080°C $\sqrt{3} \times \sqrt{3}R30°$	1100°C, 5min. $6\sqrt{3} \times 6\sqrt{3}R30°$ no $\sqrt{3} \times \sqrt{3}R30°$	1100°C, 5min. $6\sqrt{3} \times 6\sqrt{3}R30°$ no $\sqrt{3} \times \sqrt{3}R30°$	1100°C, 5min. $\sqrt{3} \times \sqrt{3}R30°$
	1150°C $6\sqrt{3} \times 6\sqrt{3}R30°$ no $\sqrt{3} \times \sqrt{3}R30°$			
1250°C, 20min. $6\sqrt{3} \times 6\sqrt{3}R30°$ $\sqrt{3} \times \sqrt{3}R30°$	1250°C, 5min. $6\sqrt{3} \times 6\sqrt{3}R30°$ no $\sqrt{3} \times \sqrt{3}R30°$			1250°C, 5min. $6\sqrt{3} \times 6\sqrt{3}R30°$ no $\sqrt{3} \times \sqrt{3}R30°$

heat transfers to the e-beam heater to reduce risk of melting (melting point is 1200°C). During heating the center of the sample plate (3 mm × 3 mm) lights up brighter than the surroundings, indicating that the highest temperature is reached at the center of the sample, and lower temperatures are at the sides.

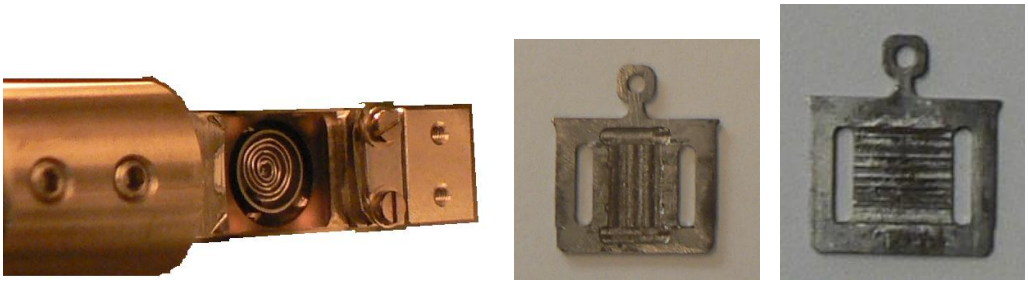

(a) **(b)** **(c)**

Figure 3.5: *a) Homebuild e-beam heater. b) Special sample plate, fitted with two slits to reduce the heat transfer towards the e-beam heater.*

Two pyrometers were used in order to monitor the temperature of the sample during heating, the handheld CHINO Comet 1000, temperature range $600-3000$°C and the IMPAC IP140, temperature range $160-1200$°C (range depends slightly on emission-factor). The use of the Comet turned out to be very difficult; many times it failed to measure any temperature, and it has on offset of (250 ± 50)°C with respect to the IP140. The IP140 is a much newer and more reliable model, so the IP140 was used. The available viewport allowed measurement of the temperature with an angle of approximately 30° with respect

to the normal of the sample. The accuracy of the measured temperature is estimated at 50°C.

3.3.2 Results and discussion

In this section the characterization of the surfaces with LEED after heat treatments are described and discussed. An overview of the performed heating experiments on these samples together with the observed LEED spectra is shown in table 3.3. LEED measurements of each sample taken between the heating treatments will no be discussed.

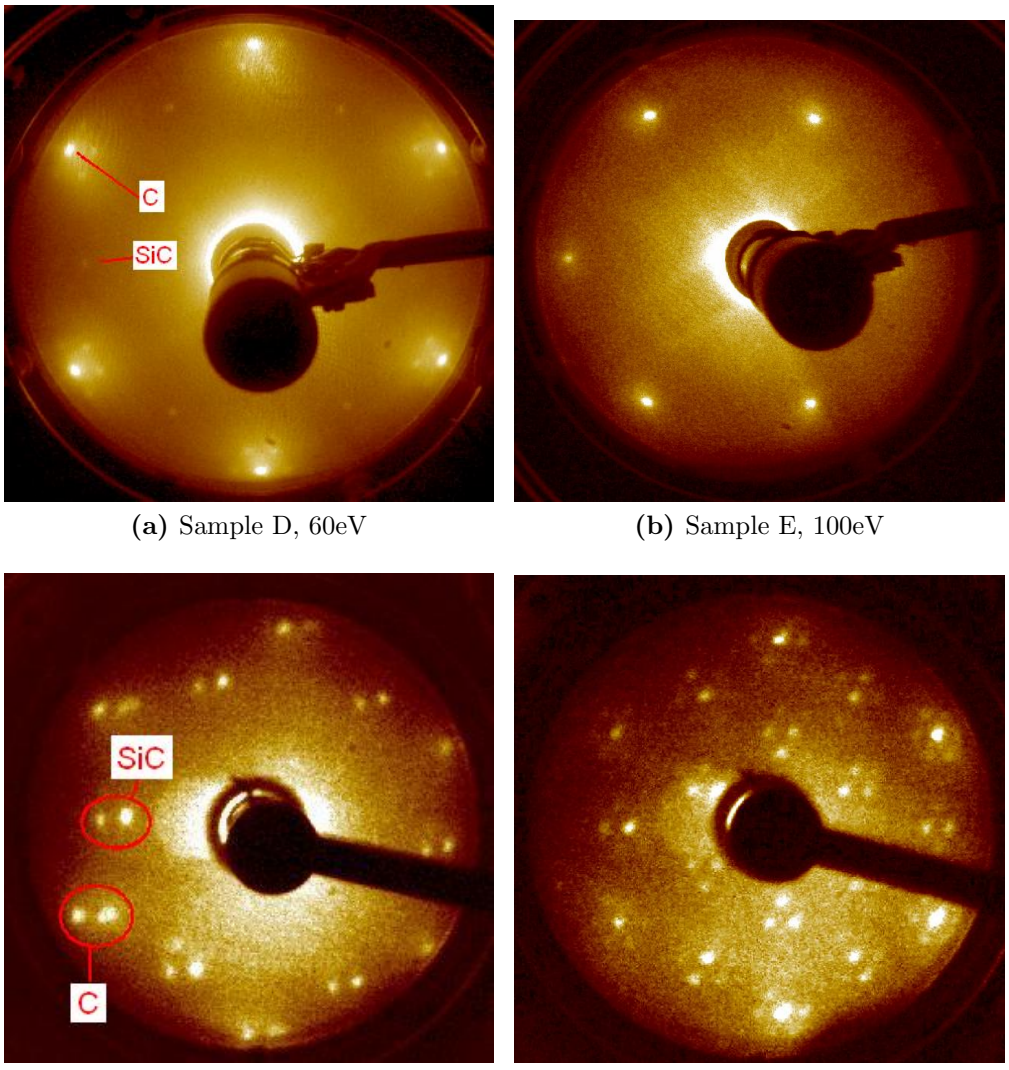

(a) Sample D, 60eV **(b)** Sample E, 100eV

(c) Sample F, 100eV **(d)** Sample G, 100eV

Figure 3.6: *LEED measurements on the indicated samples after the described heat treatments*

Sample C shows a $3\sqrt{3} \times 3\sqrt{3}R30°$ pattern in LEED after its first heat treatment

Table 3.3: *Overview of heat treatments with observed LEED patterns*

Sample C	Sample D	Sample E	Sample F	Sample G
4H-SiC $< 0.5°$ off-axis	4H-SiC $< 0.5°$ off-axis	4H-SiC $\approx 4°$ off-axis	4H-SiC $\approx 4°$ off-axis	6H-SiC $< 0.5°$ off-axis
800°C, 15min. $3\sqrt{3} \times 3\sqrt{3}R30°$		800°C, 34min. $3\sqrt{3} \times 3\sqrt{3}R30°$		1050°C, 15min. $\sqrt{3} \times \sqrt{3}R30°$
900°C, 15min. $3\sqrt{3} \times 3\sqrt{3}R30°$[1]		900°C, 3min. $3\sqrt{3} \times 3\sqrt{3}R30°$[1]		1100°C, 3min. Exposed[8] SiC 1×1
1050°C, 15min. $3\sqrt{3} \times 3\sqrt{3}R30°$[1]		1050°C, 15min. $3\sqrt{3} \times 3\sqrt{3}R30°$[15]		1050°C, 10min. $\sqrt{3} \times \sqrt{3}R30°$ $6\sqrt{3} \times 6\sqrt{3}R30°$
		1100°C, 3min.[6]	1050°C, 10min. 1100°C, 5min.[3] Very weak $6\sqrt{3} \times 6\sqrt{3}R30°$	1100°C, 3min. $\sqrt{3} \times \sqrt{3}R30°$ $6\sqrt{3} \times 6\sqrt{3}R30°$
		1150°C, 5min.[6]	1150°C, 5min.[6]	
1250°C, 30min. Graphite 1×1	1100°C, 30min.[2] 1250°C, 20min.[3] Very weak SiC 1×1 Graphite 1×1 , with 6×6[4]	1250°C, 8min.[6]	1250°C, 20min. SiC 1×1 Graphite 1×1[7]	1250°C, 4min.[9] Weak SiC 1×1 , with 6×6 Graphite 1×1 , with 6×6
		1100°C, 20min.		$6\sqrt{3} \times 6\sqrt{3}R30°$
		1220°C, 20min. Graphite 1×1		no $\sqrt{3} \times \sqrt{3}R30°$

Additional notes:

1. Heating to 900°C decreases $3\sqrt{3} \times 3\sqrt{3}R30°$ intensity relative to 1×1 intensity. Heating 1050°C decreases $3\sqrt{3} \times 3\sqrt{3}R30°$ relative intensity even further to only just observable.
2. Temperature was slowly ramped to 1100°C over a few hours.
3. Sample did not cool down between this and previous heating step.
4. SiC 1×1 intensity is weak relative to graphite 1×1, see figure 3.6a.
5. Other position on sample shows a 3×3 pattern.
6. No recognizable pattern was observed in LEED.
7. Strange LEED pattern, each spot seems to appear twice as shown in figure3.6c.
8. Due to technical problems the sample was exposed to approximately 10^{-3}mbar for about 60s.
9. During the four minutes of heating at 1250°C an overshoot occurred. Temperature during this overshoot was outside of the pyrometers range, but is estimated to be below 1350°C.

at 800°C. Additional heating at 900°C diminished the intensity of these spots. After a successive heat treatment at 1050°C the spot intensity can be hardly observed, except for the bright 1×1 spots.

This result is in agreement with the LEED pattern displayed in De Heer at al. [13] (see also table 3.2) showing a 1×1 LEED pattern after heating to 1050°C. It also agrees

with LEED patterns observed by Rollings at al. [30], which showed a 1×1 LEED pattern after heating to 1000°C. The $3\sqrt{3} \times 3\sqrt{3}R30°$ pattern observed on sample C has not been observed in literature. Possibly, this pattern could be formed by the oxygen reconstruction on the sample surface, which would not have shown an influence in the results in the papers presented in table 3.2, since there $si - flux$ was used to remove the oxygen from the samples before starting the measurements.

The last heat treatment on the sample C at 1250°C for 30min produced only graphite 1×1 spots, which is similar to the result for sample E shown in figure 3.6b). Since De Heer at al. [13] observed the SiC 1×1 spots (see figure 3.4) up to a thickness of 2.5 graphene layers, as established by Auger Electron Spectroscopy (AES), this observation on sample C indicates that there are three or more layers of graphene on the sample.

Sample D has been heated slowly to the final temperature of 1100°C over a few hours, at which it was kept for 30min afterwards. The second heating step to 1250°C for 20min was done without cooling down the sample. LEED measurements after the heat treatment showed very weak SiC 1×1 spots and graphite 1×1 spots, with a 6×6 pattern around each graphite spot, see figure3.6a. An observation of the 6×6 pattern around graphite spots have been explained in literature by double diffraction process arising from combination of a SiC and graphite reciprocal vectors [21].

The weak SiC 1×1 spots indicate that less graphite was formed on the sample D than on sample C, where no SiC 1×1 spots have been observed. By comparison with the results of de Heer at al. [13] (figure 3.4) it could be concluded that at least 2.5 graphene layers have been formed on the sample, because otherwise the 6×6 pattern around the SiC spots should also have been observed. However, quantitative comparison between LEED measurements is not possible, since the intensity has not been measured in our LEED experiments. Nevertheless, it can be concluded that there is less graphite on sample D than on sample C, which did not show SiC 1×1 spots. This is also in agreement with the fact that sample C was heated to 1250°C for 30min, whereas sample C was only heated to 1250°C for 20min, allowing less time for graphitization process.

Sample E was given heat treatments at 800°C, 900°C and 1150°C, resulting in very similar LEED patterns to sample C. However, after following heat treatment steps at 1100°C, 1150°C and 1250°C, a LEED pattern could not been observed. An additional heat treatment to 1100°C and to 1220°C, produced graphite 1×1 spots (figure 3.6b). In analogy to sample C, this indicates that there are more than 2.5 graphene layers on the sample. The comparable results of the heat treatments of samples E and C are in accordance with the comparable heating times around 1250°C, see table 3.3.

Sample F was heated to 1050°C, followed (without allowing the sample to cool down) by a heat treatment at 1100°C. This resulted in a very weak $6\sqrt{3} \times 6\sqrt{3}R30°$ pattern in LEED, which is comparable to observations in literature, where the $6\sqrt{3} \times 6\sqrt{3}R30°$ surface reconstructions starts appearing at roughly 1100°C, see table 3.2. The reason why the $6\sqrt{3} \times 6\sqrt{3}R30°$ pattern appears weakly in LEED could be that this reconstruction might not be present on the entire substrate, but only on certain parts.

After heating to 1150°C, no LEED measurement could be obtained. The reason is not known. An additional heating to 1250°C for 20min allowed again observation of the LEED

pattern, which is shown in figure 3.6c. However, two spots are present at each positions, where a single graphite 1×1 or a SiC 1×1 spot is expected. A spot splitting in LEED measurements usually represents stepped sample surface, which is accordance with the larger off-axis (4°) of the SiC(0001) surface.

Sample G was heated to 1050°C, which resulted in a $\sqrt{3} \times \sqrt{3}R30°$ LEED pattern. After heating to 1100°C some technical problems occurred and the sample was exposed to approximately 10^{-3}mbar for about a minute. Therefore another heat treatment at 1050°C was applied in order to remove a possibly formed oxide layer on the surface. The $6\sqrt{3}\times6\sqrt{3}R30°$ surface reconstruction has been observed in LEED. This reconstruction was probably formed during the heating step at 1100°C before exposing the sample to higher pressure, since heating it to an additional 1100°C did not change the LEED pattern. The appearance of the $6\sqrt{3}\times6\sqrt{3}R30°$ surface reconstruction after heating the sample to 1100°C is in agreement with the observation on sample F and also in agreement with literature.

Afterwards, sample G was heated to 1250°C for 4 min, however, an overshoot occurred shortly, which could not be measured using the pyrometer, but it is estimated to have been below 1350°C for less than 30 s. This treatment resulted in a $6\sqrt{3} \times 6\sqrt{3}R30°$ pattern in LEED, shown in figure 3.6d. This pattern is different from the pattern observed after heating to 1100°C. The SiC 1×1 spots of the pattern have decreased in intensity along with the 6×6 pattern around these spots, whereas the graphite 1×1 spots seem to have increased in intensity together with their surrounding 6×6 pattern. The $\sqrt{3} \times \sqrt{3}R30°$ spots have disappeared.

This measurement is not in agreement with those published by [13] (figure 3.4), where the $\sqrt{3} \times \sqrt{3}R30°$ spots did not disappear. However, all the other measurements from literature shown in table 3.2 have shown the same disappearance of the $\sqrt{3} \times \sqrt{3}R30°$ spots.

The intensity of the SiC 1×1 spots together with the appearance of a 6×6 pattern around the SiC 1×1 spots indicates that fewer graphite layers were formed on sample G than on samples C,D,E and F. A comparison with the results of De Heer et al. [13] (figure 3.4) would lead to the estimation of the formation one or two graphene layers on the sanmple.

3.3.3 Conclusions

A final heat treatment on sample G of 1250°C for 4min resulted in LEED patterns comparable to the results shown in De Heer [13], indicating that one or more graphene layers have been grown on the sample.

Longer final heat treatments, such as heating to 1250°C for 20 min, which were performed on sample D and F, gave rise to LEED patterns with mainly graphite 1×1 spots and weak SiC 1×1 spots. Confrontation with the results by De Heer et al. [13] implies that probably 3 or more graphene layers have been formed.

Even longer heating treatments, such as heating to 1250°C for 30 min or heating to 1250°C for 8 min followed by heating to 1220°C for 20 min, as were performed on samples A and E respectively, resulted in LEED patterns, which showed the 1×1 spots related to

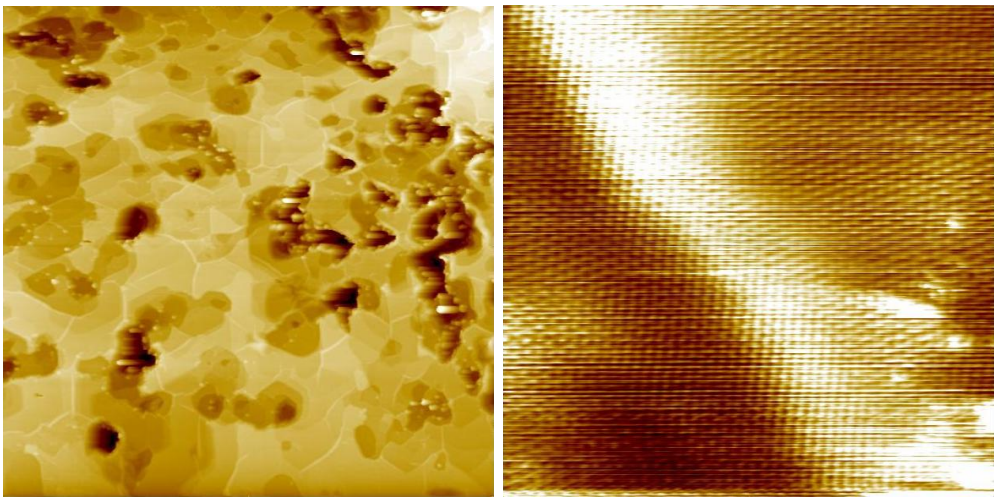

(a) **(b)**

Figure 3.7: *a) A* 1000nm × 1000nm *STM image taken on sample C at* V_{bias} = 1.0V *and* $I_{setpoint}$ = 0.23nA. *b)* 10nm × 10nm *STM image taken on sample F at* V_{bias} = 20mV *and* $I_{setpoint}$ = 3.2nA.

graphite. This indicates that there ware many layers of graphene on the sample, i.e. more than the number of layers on samples D and F.

3.4 STM characterization

After performing the heat treatment on the samples, it is expected that conductive graphene layers have been formed. This can be confirmed using STM measurements, which also reveal information on the morphology of the sample.

3.4.1 General morphology

After applying the heat treatment, the morphology of the sample changes from the morphology seen in the AFM images after etching, see figure 3.3, into the morphology shown in figure 3.7a. The large terraces, which were observed in AFM before the heat treatment are no longer observed, instead smaller atomically flat regions show up, which do not show aligned step edges. The step edges, ranging in height from $0.3 - 5$nm observed after the heat treatment appear randomly. This morphology, shown in figure 3.7a for sample C, has also been observed on samples D, E and F. STM images of sample G generally show many bumps, which are roughly 3nm high, see figure 3.8a. However, a part on sample G was found which did not show these bumps and an STM image taken on this part, shown in figure 3.8b, shows the same morphology as the other samples.

Another feature of the graphene layer(s) on the samples is that no sharp step edges have been observed in STM. In stead the graphene layers seem to have grown continuously

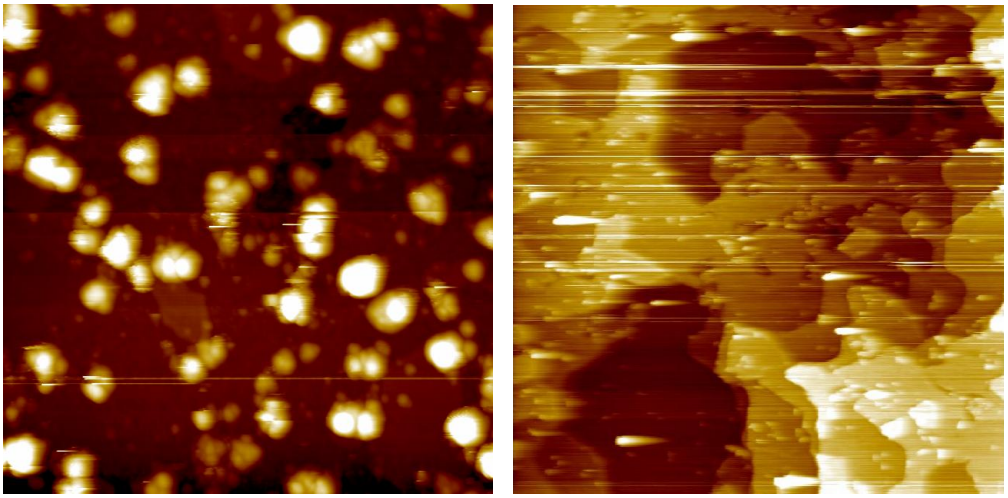

(a) **(b)**

Figure 3.8: *a) A* 144nm × 144nm *STM image taken on sample C at* $T = 5\text{K}$, $V_{bias} = -8.1\text{V}$ *and* $I_{setpoint} = 46\text{pA}$. *b) A* 200nm × 200nm *STM image taken on sample G at* $V_{bias} = 1.0\text{V}$ *and* $I_{setpoint} = 1.83\text{nA}$.

over the step edges. An STM image in which such continuous growth is observed is shown in figure 3.7b.

Both the smaller atomically flat regions with the random step edges and the continues graphene layer have also been observed in Seyller [32]. So far, no explanation for the observed morphology is known.

3.4.2 Atomic resolution

STM images taken on a small range are able to show the atomic corrugation of the graphene layer for all samples, for example see figure 3.9. This confirms that graphene has been grown on all the samples. The atomic corrugation can appear differently using different parameters. In figure 3.9a taken at $V_{bias} = 0.90\text{V}$ the hexagons appear in the image, while in figure 3.9b taken at $V_{bias} = -0.71\text{V}$ a triangular mesh appears in the image.

The triangular mesh seems similar to the mesh observed on graphite. In graphite, the A-B symmetry within the graphene unit cell is broken by the stacking formation of the graphene layers in the graphite, where an atom on an A-site in the top layer is always positioned above an atom in the underlying layer, while an atom on a B site in the top layer is not. STM images of graphite always reveal a triangular atomic mesh. This explanation could also be applicable for two graphene layers or more.

However this cannot fully explain the triangular mesh shown in figure 3.9b, since a different bias measured at the same position reveals a hexagonal mesh. It is possible that electronic states at certain bias voltages have A-B symmetry, while others at different bias voltages do not.

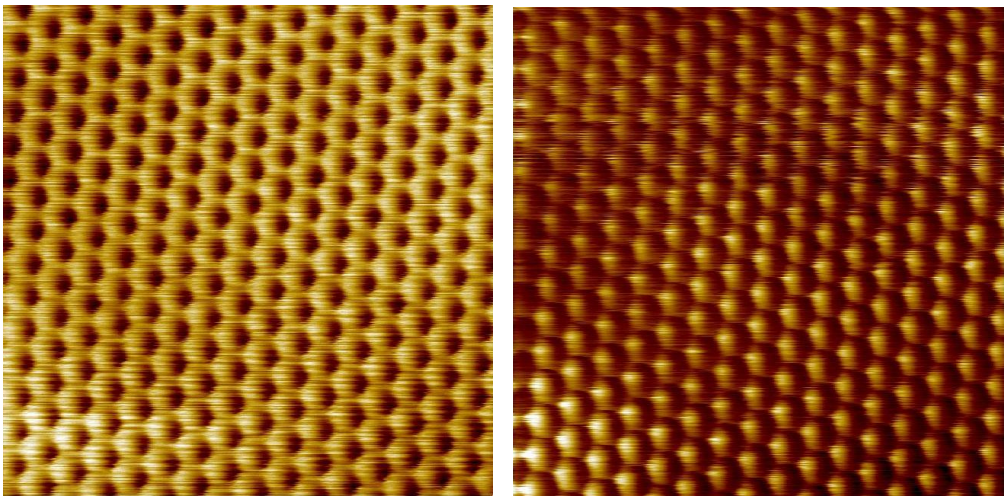

(a) **(b)**

Figure 3.9: *Two* 3.8nm × 3.8nm *STM measurements taken at T=77 K at the same position on sample F, but at different bias voltage. a) Is taken at* $V_{bias} = 0.90\text{V}$ *and* $I_{setpoint} = 1.1\text{nA}$ *and b) at* $V_{bias} = -0.71\text{V}$ *and* $I_{setpoint} = 1.1\text{nA}$.

From the measured data no clear relation has been established yet revealing on which samples/with how many graphene layers and at which bias voltage the triangular or the hexagonal lattice is measured.

3.4.3 Nanomesh

Next to the atomic corrugation another corrugation is observed in STM images of a slightly larger scale as shown in figure 3.10. This corrugation, which will be referred to as the nanomesh, appears to be a hexagonal mesh with a lattice constant ≈ 20Å rotated 30° with respect to the graphene mesh. A more detailed discussion of the nanomesh will be given in section 4.1.1. The nanomesh has been observed on samples D, F and G, where it seemed easy to see the nanomesh in images obtained on sample G, and much more difficult to see them on images obtained on D and F.

Since the nanomesh is an effect caused by the interface between the graphene and the SiC, it is expected to show less influence with an increasing number of graphene layers. Thus it can be concluded that on samples C and E, on which no nanomesh has been observed, there are more graphene layers present than on samples D, F and G. And that there are probably more layers of graphene on samples D and F than on G, since on sample G the nanomesh was the most easily detectable.

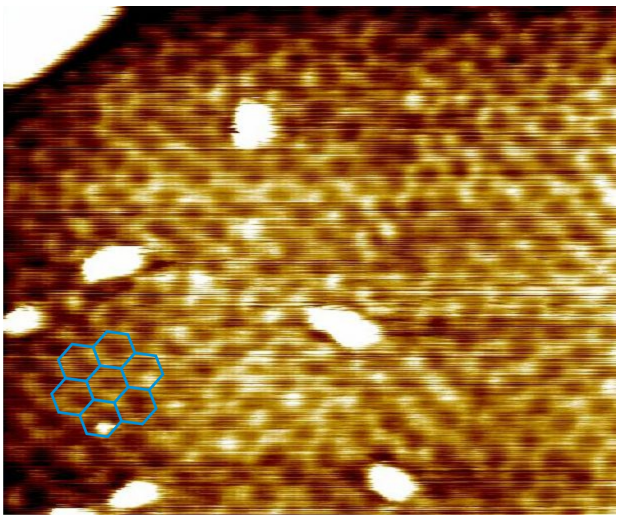

Figure 3.10: *A* 35nm × 35nm *STM image taken on sample G at* $V_{bias} = 1.0\text{V}$ *and* $I_{setpoint} = 1.83\text{nA}$. *A few hexagons of the nanomesh are highlighted in blue.*

3.4.4 Conclusions

The heat treatment causes a change in morphology from large atomically flat terraces with aligned step edges, to smaller atomically flat regions with random step edges. The graphene layer remains continuous over large regions, even over step edges.

The graphene atomic corrugation has been observed on all samples, either as a triangular or hexagonal mesh. This confirms that graphene has been formed on all samples.

A corrugation with a lattice constant $\approx 20\text{Å}$ rotated 30° with respect to the graphene atomic mesh, called the nanomesh, has been observed for samples D, F and G. Where on sample G the nanomesh seems to be more easily detectable in STM. This indicates that there are more layers of graphene on samples D, F and G than on sample C and E, and that there are probably also more layers of graphene on samples D and F than on G.

3.5 General conclusions

SiC(0001) surfaces with large atomically flat areas can be obtained from polished SiC using hydrogen etching.

Applying heat treatments to SiC samples successfully produces graphene layers.

Layer thickness has been established to increase with the duration of the final heating step at $\sim 1250°\text{C}$.

Chapter 4

Results

4.1 STM/STS Results

STM images have been taken on sample G at three different locations. Images taken at these different locations can be divided in regions A,B and C. These regions are characterized by their topographic features. An STM image containing all three regions is shown in figure 4.1a. The three different regions will be called A,B and C and are illustrated in figure 4.1b.

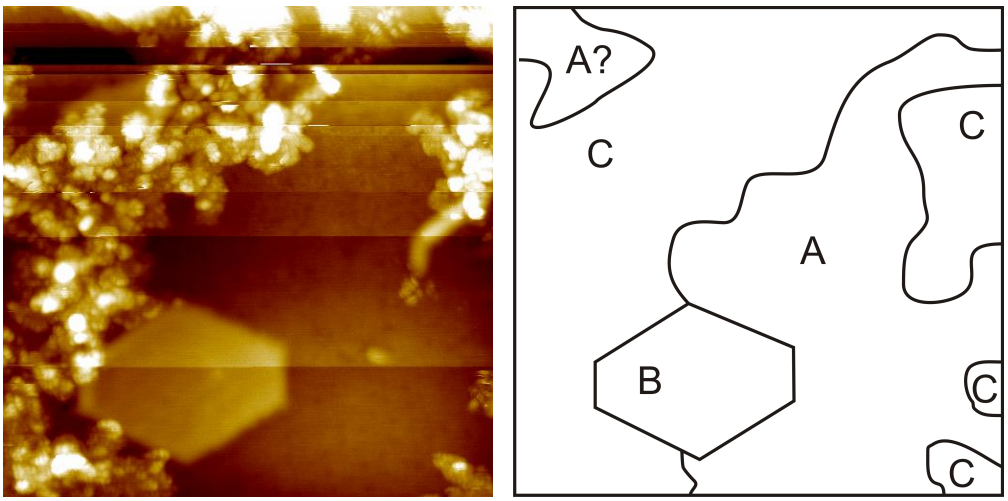

(a) 3V, 50pA **(b)**

Figure 4.1: *a) A* 50nm × 50nm *STM image taken on sample G at* $T = 5$K, $V_{bias} = 3.0$V *and* $I_{setpoint} = 50$pA. *b) A schematic drawing of the same image denoting three different regions, A,B and C.*

The difference between regions A, B and region C can be clearly observed in figure 4.1a. While region A and B are both very flat (the Root Mean Square(RMS) of the height in these region has been measured to be $\approx$ 50pm), region C is very rough (a RMS of

the height in this region has been measured to be ≈ 200pm). The features appearing in region C are also very disordered. Possibly, this is a region where the graphene formation process has not been fully completed yet. The differences between regions A and B are less apparent in figure 4.1a, but will be pointed out using smaller scale STM images and STS measurements in the rest of this section.

Region A, B and C appear in a ratio of 4 : 1 : 2 in the measurements at five different positions on the sample.

4.1.1 Region B

Firstly, region B is studied in more detail. One of the STM images taken on region B is depicted in figure 4.2. This image shows a hexagonal mesh, as accentuated by the white hexagons drawn in the figure. This hexagonal mesh is characterized by a lattice constant of $a = 2.45$Å, which is the lattice constant of graphene. This is a clear indication that graphene has been formed on the sample. However, it is not yet clear whether this is a single layer of graphene.

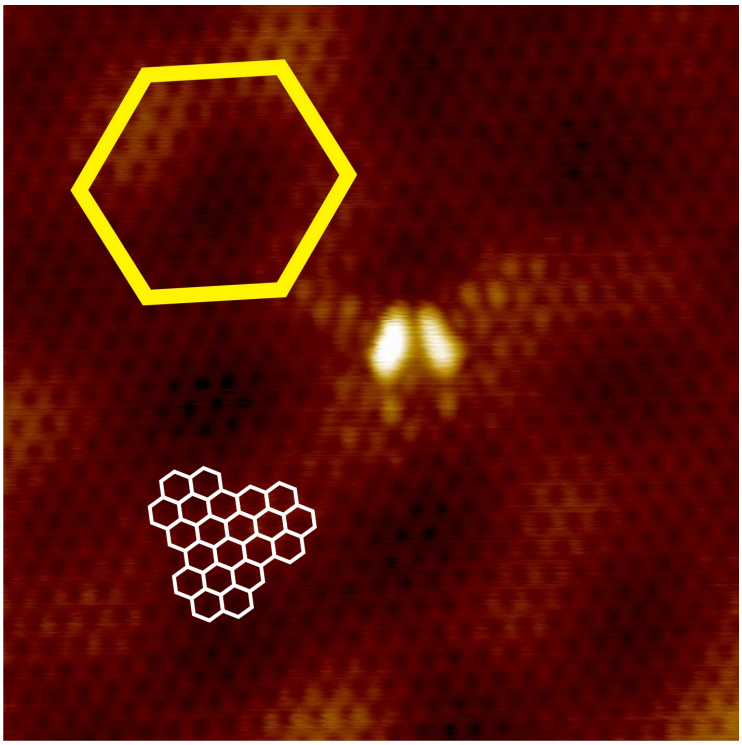

Figure 4.2: *A* 7nm × 7nm *STM image taken on sample G at* $T = 5$K, $V_{bias} = 300$mV *and* $I_{setpoint} = 45$pA. *The white hexagons illustrate the hexagonal atomic mesh of the graphene layer and the yellow hexagon illustrates the hexagonal nanomesh.*

Figure 4.2 also reveals a larger hexagonal mesh, which is called the nanomesh. This nanomesh structure is characterized by a lattice constant of ≈ 20Å and is rotated 30° with

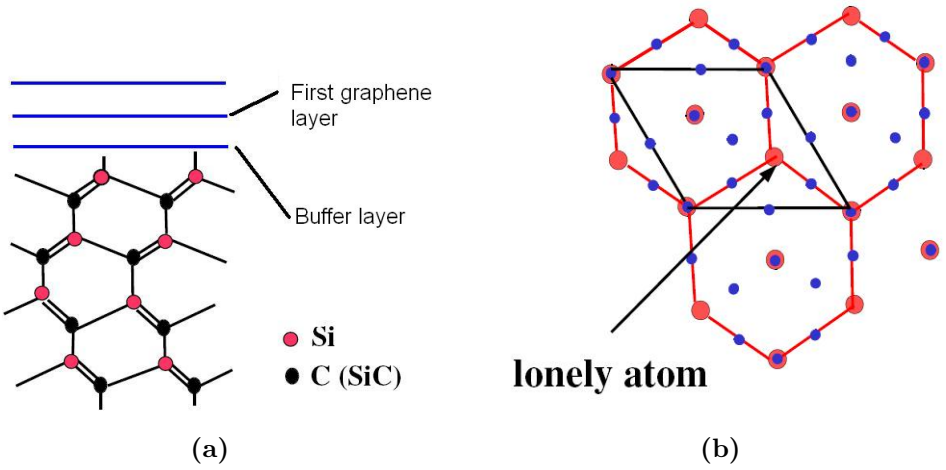

Figure 4.3: *Schematic representations of a possible buffer layer [31] situated between the silicon terminated Si(0001) and the first graphene layer. a) Shows a side view while b) shows a topview.*

.

respect to the graphene hexagonal mesh. This means that the nanomesh is aligned with the SiC atomic mesh and that its lattice constant is approximately six times as large as the lattice constant of the SiC triangular atomic mesh(3.1Å). Thus, the nanomesh would show up in LEED measurements as a 6×6 pattern. Such 6×6 patterns have been observed around the SiC 1×1 spots and the graphite 1×1 spots in LEED, as shown in figure 3.6d.

A freestanding graphene layer(s) is not expected to show a feature such as the nanomesh, so this nanomesh is related to the interaction between the graphene layer(s) and the substrate. Unfortunately, the structure of the substrate near the interface between the substrate and the graphene is not yet well understood. It is generally expected that the top layer of the substrate is a layer above the silicon terminated SiC(0001) surface as drawn in figure 4.3a. This layer will be referred to as the buffer layer, and is distinguished from the first graphene layer by the band structure, which is not linear like that of graphene. Different models describing the structure of the buffer layer have been published [25, 31]. However, it is difficult to relate these models to the experimental observation of the nanomesh for two reasons. Firstly, calculating the influence of a suggested model is typically done using Local Density Approximation (LDA) electronic structure calculations. Such calculations are not able to handle the large unit cell required to describe the nanomesh. Secondly, the nanomesh coincides with the Moiree pattern formed by the triangular mesh of the silicon terminated SiC(0001) surfaces and the hexagonal mesh of the graphene. Therefore it is difficult to relate the nanomesh to any specific model for the buffer layer.

4.1.2 Region A

A detailed study of region A reveals that STM images taken on this region show the same structure anywhere on region A. Such an STM images is shown in figure 4.4. This image shows many bright features, such as the bright feature marked by the blue circle, which do not appear to show an ordered structure. In between these bright features the hexagonal graphene atomic mesh can be observed, with a lattice constant $a = 2.45$Å as expected for graphene. A region where this can be observed is indicated by the white circle. A few hexagons of the atomic mesh have been drawn in white to help the eye.

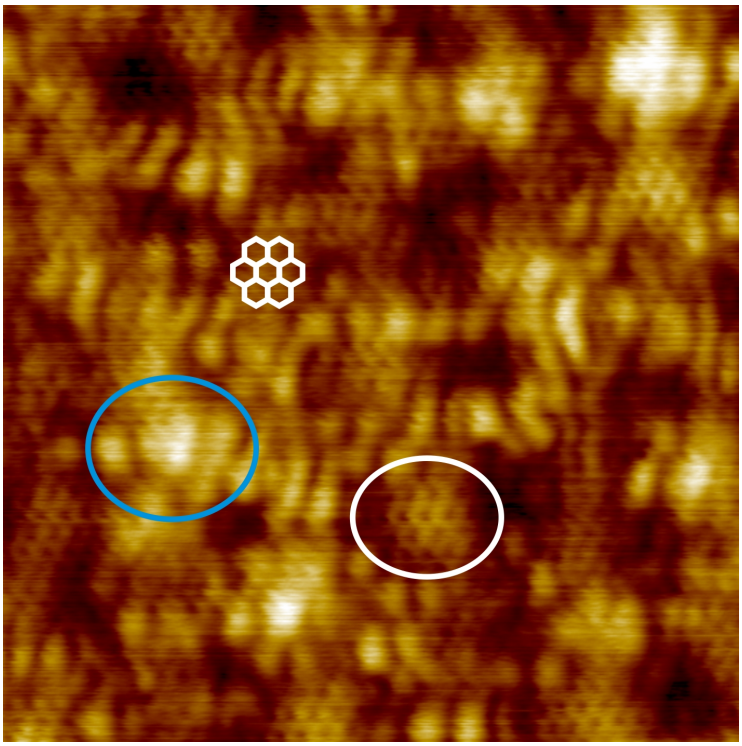

Figure 4.4: *A* 10nm × 10nm *STM image taken on sample G at* $T = 5$K, $V_{bias} = 300$mV *and* $I_{setpoint} = 47$pA. *The white hexagons illustrate the hexagonal atomic mesh of the graphene layer and the white circle shows a part of the image where the atomic hexagonal mesh is also visible. The blue circle shows the bright features.*

More information about the origin of the bright features is revealed in STM images taken at different bias voltages, such as shown in figure 4.5. These images, which were taken on a different part of the substrate, show that these bright features disappear when scanning at bias voltages close to zero, and will be discussed in sequence going from high bias ($V_{bias} = 400$mV) toward low bias ($V_{bias} = -400$mV).

Images 4.5d and 4.5c, taken at $V_{bias} = 400$mV and $V_{bias} = 300$mV respectively, show the same bright features as seen in figure 4.4. This makes clear that the part of the substrate studied in figure 4.5 is in fact similar the the image shown in figure 4.4. Comparing image 4.5d to image 4.5c, shows that some of the bright features in image 4.5d have disappeared

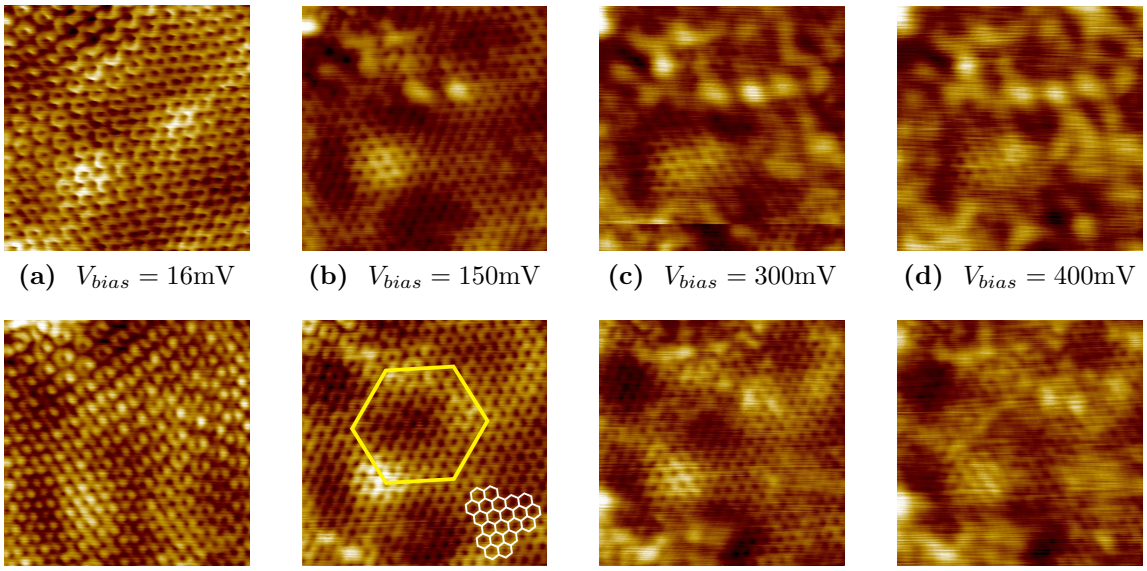

(a) $V_{bias} = 16\text{mV}$ **(b)** $V_{bias} = 150\text{mV}$ **(c)** $V_{bias} = 300\text{mV}$ **(d)** $V_{bias} = 400\text{mV}$

(e) $V_{bias} = -16\text{mV}$ **(f)** $V_{bias} = -150\text{mV}$ **(g)** $V_{bias} = -300\text{mV}$ **(h)** $V_{bias} = -400\text{mV}$

Figure 4.5: 5nm × 5nm *STM images taken on an A type region on a different part of the substrate. All were taken at the same position and with* $I_{setpoint} = 38\text{pA}$*, but at different bias voltages. The white hexagons in f) illustrate the hexagonal atomic mesh of the graphene layer and the yellow hexagon in f) illustrates the hexagonal nanomesh.*

in image 4.5c, while other features have decreased their intensity.

Image 4.5b, taken at $V_{bias} = 150\text{mV}$, shows even less of the bright features. One feature in the top left corner of the image still remains as bright as in image 4.5d taken at $V_{bias} = 150\text{mV}$. The rest of the image shows, that the bright features, which have disappeared have been replaced by the atomic hexagonal mesh of graphene (a few hexagons of this mesh have been drawn in image 4.5f). This shows that at the positions where at high bias, see image 4.5d, bright features are observed, the atoms are still arranged as a graphene layer. Therefore the bright features must be related to the electronic structure and not the atomic arrangement.

Image 4.5a, taken at $V_{bias} = 16\text{mV}$, shows none of the bright features observed in image 4.5d. In stead, it shows a pattern related to scattering on an atomic scale defect as explained in [43, 44]. Next to this pattern, three new bright features emerge. These features occur on three corners of a hexagon associated with the nanomesh. This hexagon is drawn in yellow in image 4.5f. However the bright features could also be related to scattering from a atomic scale defect in a graphene layer, as described in [41].

Image 4.5e, taken at $V_{bias} = -16\text{mV}$ show a similar pattern as observed at $V_{bias} = 16\text{mV}$. However the positions of the three bright features seem to have moved. This can be explained by scattering from a atomic scale defect in a graphene layer, as described in [41].

Image 4.5f, taken at $V_{bias} = -150\text{mV}$ shows the hexagonal atomic mesh in nearly the entire image. In the top left of the image the pattern associated with scattering from an

atomic defect is visible. The nanomesh in this image can be made out as being hexagonal with a lattice constant of ≈ 21Å, consistent with that of the nanomesh observed on region B. The hexagon is drawn in the image in the yellow. Although an entire hexagonal can be observed, three corners of the hexagon seem to show more intensity. These are the same corners as observed in image 4.5a. To the bottom left of the image two new bright features emerge.

Image 4.5g, taken at $V_{bias} = -300$mV shows already more bright features, and image 4.5h, taken at $V_{bias} = -400$mV shows even more bright features. Apparently bright features emerge at lower bias voltages. Similar to the appearance of bright features at higher positive bias voltages($V_{bias} \geq 300$mV).

So far, it has been established that the bright features are related to electronic states. Such electronic states are not visible at bias voltage close to zero. The position of the bright features shown in figures 4.4 and 4.5, indicated in figure 4.4 by the blue circle, do not show an apparent structure. However, FFT analysis applied on a larger scale image taken at $V_{bias} = 300$meV reveals that the bright features show three spots in FFT which have also been observed in LEED. These three spots are indicated by the green circle in figure 4.6 which shows a LEED measurement done on sample G. The three spots are the three spots in the $6\sqrt{3} \times 6\sqrt{3}R30°$ pattern nearest to the first order $\sqrt{3} \times \sqrt{3}R30°$ spots.

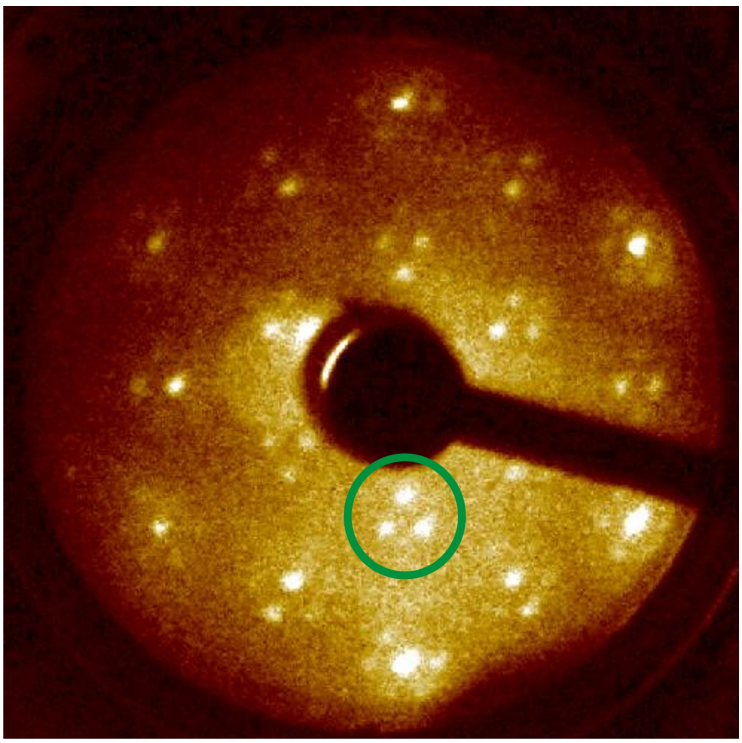

Figure 4.6: *A LEED measurement of Sample G at* $E_0 = 100$ev. *The three spots caused by the bright features have been indicated with a green circle.*

The observation that the bright features are electronic states which show up as spots

close to the $\sqrt{3} \times \sqrt{3}R30°$ spots in LEED possibly reveals more information about the buffer layer. The appearance of such states can be explained using the model for the buffer layer proposed in [31], see also figure 4.3. The proposed layer is a carbon layer with the same atomic mesh as a graphene layer (which in [31] has been taken to be slightly (8%), stretched in order to speed up calculations). In this model not all silicon atoms of the SiC(0001) surface are able to bond with a carbon atom and a few dangling bonds remain. These dangling bonds are suggested to form a $\sqrt{3} \times \sqrt{3}R30°$ pattern. In view of these results it is possible that the bright features observed in STM are caused by dangling bonds of silicon atoms of the SiC(0001) surface. This would not yet explain why three spots close to the $\sqrt{3} \times \sqrt{3}R30°$ pattern are observed and not the $\sqrt{3} \times \sqrt{3}R30°$ pattern itself. However, it is not possible to approach this problem using an LDA model, since this would require a too large unit cell.

4.1.3 A comparison between regions A and B

Since the local topography of regions A and B have been discussed, a comparison between these two regions can be made. Such a comparison becomes much simpler since the the graphene atomic mesh on both region A and region B is observed. The difference between region A and B is thereby reduced to a difference in number of graphene layers in either region.

A hint which region contains most graphene layers has already been presented in the form of the bright features observed in region A. The bright features are related to the buffer layer and have not been observed in region B. Additional layers of graphene are expected to screen influences of the buffer layer, so region B must have additional layers preventing the observation of the bright features. This statement will be supported by the STS measurements presented in section 4.1.4.

Another difference between A and B becomes apparent in an STM image on which both regions are visible, such as shown in figure 4.1a. A zoom in on the part where region A and B are both visible is shown in figure 4.7a. In this image, region B appears much brighter than region A, suggesting that there is a height difference between these two regions.

In figure 4.7b three cross-sections taken perpendicular to the step between region A and region B are shown. The displayed cross-sections show that region B appears to be elevated with respect to region A by $\approx$ 300pm.

The observed height difference in STM can only be understood if a proper electronic structure calculation can provide a detailed picture of the electron DOS for one and more graphene layers.

4.1.4 Spectroscopy

STS measurement were performed on regions A and B as shown in figure 4.8. Such STS plots show the local density of states which is related to the electronic band structure. Only a few experimental photoemission studies have been performed revealing information of the interface formation [48] and two studies [17, **?**][39] showing that the two Dirac cones

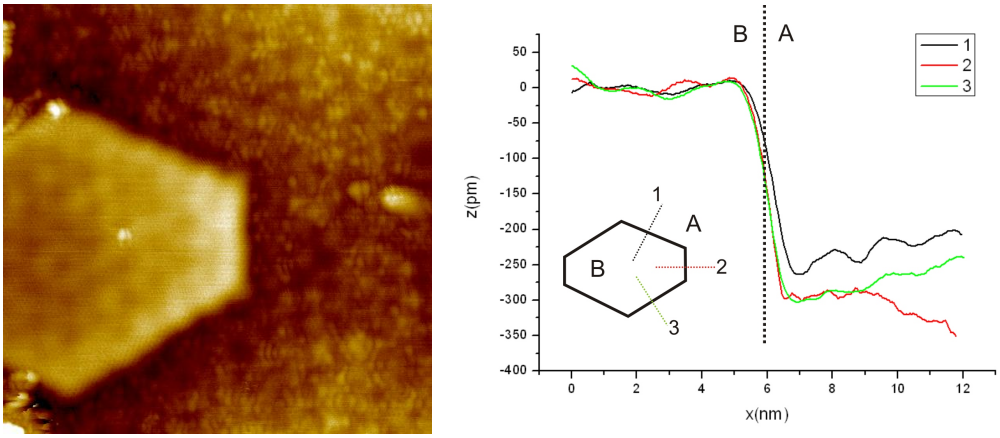

(a) (b)

Figure 4.7: *a) A* 25nm × 25nm *STM image taken on sample G at* $T = 5\text{K}$, $V_{bias} = 300\text{mV}$ *and* $I_{setpoint} = 51\text{pA}$. *b) Averaged cross-sections on lines 1,2 and 3 as shown in the inset. The averaging has been done over all the cross-sections parallel to lines 1, 2 and 3 respectively, which still intersect with the same edge of region B.*

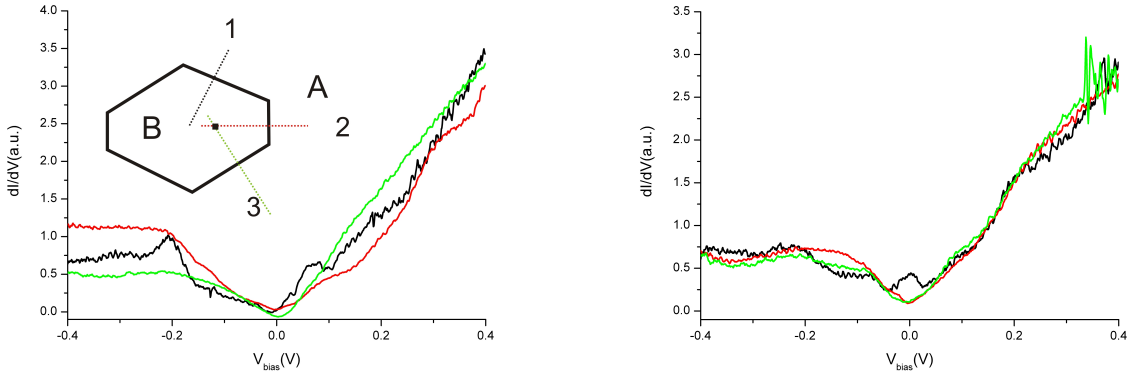

(a) (b)

Figure 4.8: *Results from STS measurements taken on three different lines are shown. The inset of a) indicates where these three lines were located. The black dot in region B indicates the centrally located defect in this region. a) Shows a spatial average over all points measured on region A for the three different lines b) Shows the same data for region B.*

have a linear dispersion in k-space. However,the cones are separated from each other with an energy gap of 0.26eV and the Dirac point is situated to 0.4eV binding energy. The shift of the Dirac point E_D is due to the electron doping of the graphene layer grown on SiC(0001), see figure 4.9a.

The photoemission measurements for the bilayer graphene [40, 39] indicate a shift of the Dirac cone by $E_D = 300\text{meV}$, and a band gap opening up of $E_G = -150\text{meV}$. Due to the

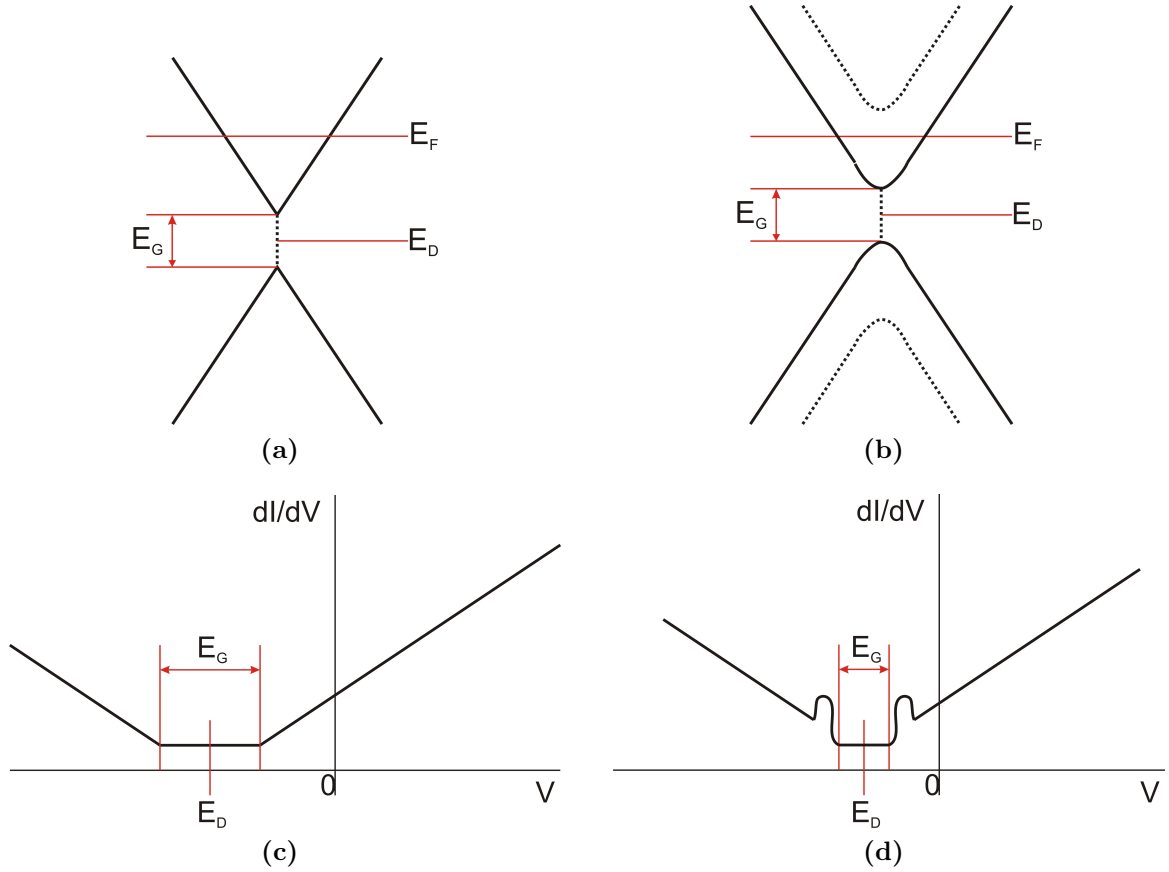

Figure 4.9: *Diagrams of the band structure a,b) and their related expectation for the density of states c,d) for a,c) single and b,d) bilayer graphene*

interaction between the two graphene layers, the dispersion relation near the Dirac point is no longer linear but shows a quadratic behavior. One expects a small energy splitting between the cones if the symmetry between the A- and B sublattice is broken, e.g. in the case of the bilayer formation. However, de Heer et al [39], showed that this already the case for the first graphene layer, resulting probably due to a different interaction of the sublattice C-atoms with the underlying bufferlayer. The resulting band structure for bilayer graphene is shown in figure, in which the dotted cones are related to the second graphene layer. 4.9b and the resulting expectation for the density of states is shown in figure 4.9d.

The measured STS spectra on regions A and B, see figure 4.8, do not show any resemblance either to the expectation for a single layer of graphene nor to the expectation for a bilayer of graphene. Due to the observation of SiC spots in LEED measurements (section 3.3) the observation of an hexagonal atomic mesh in STM measurements (sections 4.1.2 and 4.1.1) and the observation of the influence of the buffer layer in STM measurements on region A (section 4.1.2), it is not expected that both region A and B have more than two layers of graphene. It is also not expected that either region shows less than a single

layer of graphene. Therefore it can be concluded that the simple spatial average of STS measurements, see figure 4.8 does not mimic the total density of states, see figures 4.9c and 4.9d.A proper STS measurement of the total density of states would have to come from a set of STS spectra measured with an equal tip to substrate distance. However, in STS measurements the tip to substrate distance is chosen such that at the bias voltage, the current setpoint is reached. If, due to localized states, this current setpoint is reached at different tip to substrate distances depending on the measurement position, then the requirement of equal tip to substrate distances is no longer met. Results from a simple averaging of such STS measurements are then very difficult to interpret. Another explanation is that the buffer layer obscured the measured DOS of graphene. In figure 4.5 it was shown that the topography shows more the graphene layer structure for low V_{bias} and the bright features, relating to electron states of the buffer layer, at V_{bias} values above 100meV. So the dI/dV plot (shown in figure 4.8) taken at $V_{bias} = 300$meV, could therefore image the LDOS of the buffer layer.

STS result comparison to the literature

Only a few papers have been published discussing the STS measurements on graphene on SiC [26][41].

Rutter [41] reports STM and STS measurements on bilayer graphene. The number of layers has been measured by "counting the number of atomic steps from the substrate level combined with STS measurements". The resulting measurements show a topography as shown in figure 4.10a. The paper discussed dI/dV maps close to defects. In these maps a linear energy dispersion of states near the Fermi energy (within 100meV) has been observed, as shown in figure 4.10b. The slope of this dispersion is consistent with the expected $\gamma = 6.5\text{eV} \cdot \text{Å}$. Extrapolation of this dispersion leads to $E_D = (330 \pm 20)$meV, consistent with bilayer graphene. Unfortunately, if a band gap is taken into account for single layer graphene, $E_D = (330 \pm 20)$meV is also consistent with single layer graphene.

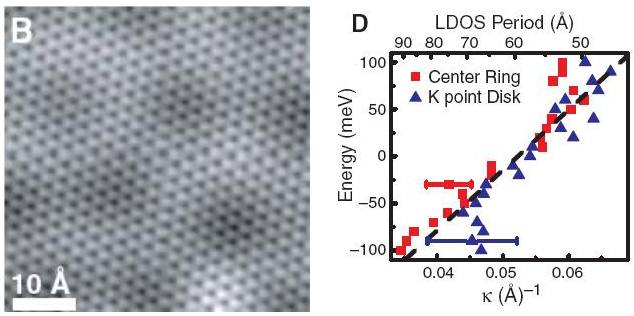

(a) **(b)**

Figure 4.10: *Measurements from [41]. a) An STM image taken on bilayer graphene at $T =$ 4.3K, $V_{bias} = 300$mV and $I_{setpoint} = 100$pA. b) A fit of the dispersion relation from Fourier transformed dI/dV maps near defects.*

The topographic STM image obtained is very similar to the STM image taken on region B, see figure 4.2, taken at the same bias voltage, $V_{bias} = 300$mV. However, the presented determination of the number of layers, i) by counting the number of layers, is doubtful since the DOS can change during the growth of graphene, as discussed in section 4.1.3, and ii) by STS measurements seems also giving the expected LDOS as is discussed in section 4.1.4

In fig 4.10 b the LDOS over a large real space region has been measured and by a Fourier transformation converted to reciprocal space, so that an energy versus momentum is obtained. The linear dispersion measurements is a very good indication that graphene has actually been observed, unfortunately the extrapolated $E_D = (330 \pm 20)$meV is not very conclusive in establishing a number of layers. It is interesting to note that the used bias voltage was small (100 meV), corresponding to a graphene STM topography picture (see fig 4.5) which does not show bright features, so that the measured LDOS is an image of the LDOS of graphene.

In **Brar** [26] STM measurements on both single and bilayer graphene have been discussed. Two different regions were observed, 1L and 2L regions. The spatial frequency of 1L and 2L regions observed in STM has been correlated to the abundance of single layer and bilayer states measured using ARPES to establish the number of layers. STM images taken at higher bias voltages, i.e. -500mV compared to -50mV, show the appearance of trimer features similar as we have found. Spatial averages of STS data for 1L and 2L regions, shown in figure 4.11, show a gap-like feature around E_F, similar as we have obtained as shown in fig. 4.8. For this gap-like feature there is no good explanation up to now.

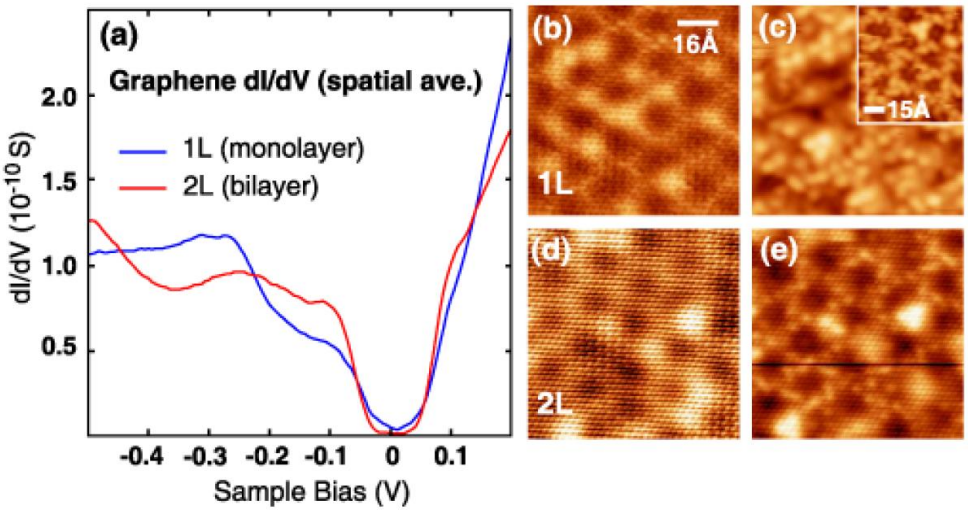

Figure 4.11: *Measurements from [26]. a) Spatially averaged dI/dV spectra of graphene monolayer and bilayer regions. b,d) Low bias images of monolayer and bilayer regions respectively (-0.05V, 0.025nA). c,e) The same regions measured at higher bias (-0.5V, 0.025nA). Inset: Image of monolayer region at an even higher bias (-1.0V, 0.003nA).*

The measured STM images, see figure 4.11, are obtained at slightly different bias voltages compared to our measurements on sample G. However region 1L, measured at

$V_{bias} = 500$meV, does resemble region A, measured at $V_{bias} = 300$meV (figure 4.4, and region 2L measured at $V_{bias} = 500$meV does resemble region B, measured at $V_{bias} = 300$meV (figure 4.2). The observation of trimers showing up at high voltage is similar to the observation of bright features showing up at higher bias on sample G (figure 4.5). Although the bright features in figure 4.5 do not necessarily appear in trimer formation. The measured STS spectra shown in figure 4.11 show similar features as STS spectra measured on sample G, shown in 4.8. This also indicates that the 1L regions correspond to A regions on sample G and that 2L regions correspond to B regions.

4.1.5 Conclusions

Sample G has been researched using STM and it was found that the surface is divided into three regions, A,B and C occurring in a ratio of $4 : 1 : 2$.

Region C seems unstructured, while region A and B both show both the hexagonal atomic mesh and the nanomesh. Both regions A and B must therefor consist of graphene.

A bias dependent STM-topography image of region A has been obtained. At low bias voltages the graphene lattice is visible whereas at higher voltages bright features, related to electron states of the bufferlayer, dominate the image. The STS plots at Vbias=300 meV resemble an asymmetric LDOS around the Fermi-level and a gap like structure around the Fermi-level. Possibly, single layer and double layer graphene are formed at the surface.

4.2 HREELS Results

In order to answer the question if a graphene layer grown on a SiC(0001) substrate behaves as a free standing graphene layer, the electronic structure and the vibrational performance is important. In the previous section, mainly the formed structures and the electronic characteristics have been discussed and in the following paragraph the phonon structure of the grown layers on SiC(0001) will be presented and discussed.

4.2.1 Measurement parameters

All presented measurements were taken at a beam energy of 20V. The sample was laterally orientated using LEED to measure the phonon dispersion in the $\Gamma - M$ direction of the graphene layer[1], with $\approx 2^\circ$ accuracy. The measurement setup was optimized by using a Cu(100) sample, achieving a countrate of 31.5kcps and a FWHM of 5.1mV at the specular position, $\theta_i = \theta_s = 59^\circ$. This rather low countrate (typically countrates of $100-150$kcps are obtained) is probably due to the corrugated surface of the Cu(100) sample. All presented measurements were obtained at a scattering angle of $\theta_s = 69^\circ$. Off specular measurements were taken at different lower incoming electron angles, $\theta_i < \theta_s = 69^\circ$.

[1]Note that this is the $\Gamma - K$ direction relative to the SiC

Measurements were conducted at two positions on the sample, one position outside the center, and a position near the center to compare the possible effects of the inhomogeneous heat treatment, as were discussed in section 3.3.1. The measurements show different features, attributed to a hot spot at the center of the substrate roughly 3mm in diameter.

4.2.2 Measurements outside the center

In figure 4.12 measurements were taken outside the center of sample E are shown for different scattering geometries.

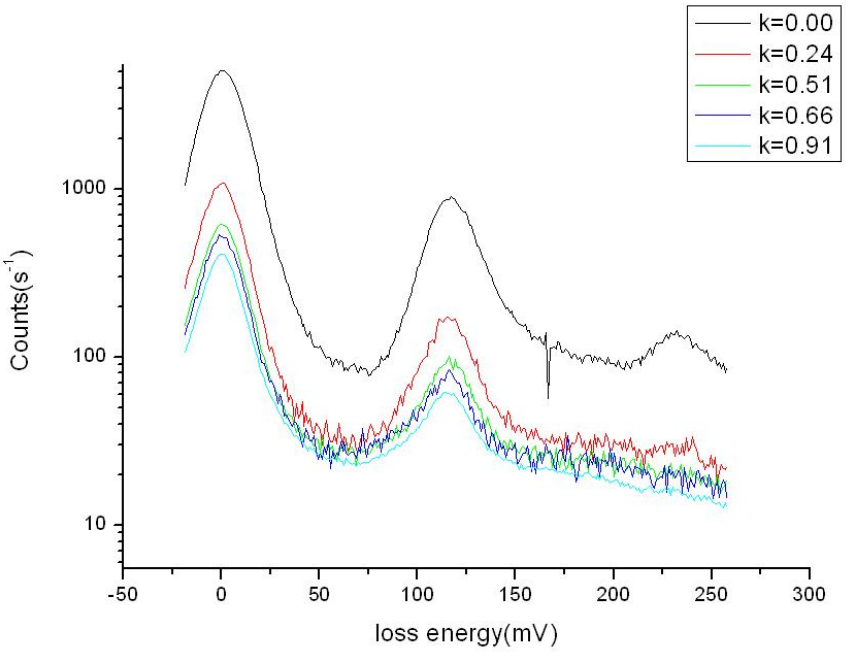

Figure 4.12: *Energy loss spectra taken outside the center of sample E at different momentum transfer(denoted in* $\mathring{A}^{-1}$*).*

The specular measurement has a very broad elastic peak with countrate 5.1kcps and a FWHM of 23meV. This FWHM is much larger than the resolution of the HREELS setup (the measurement on the copper sample shows a FWHM of 5.1meV). A similar broadening has observed for for Si 7×7 surfaces [16]. This has been explained [16] in relation to the presence of silicon dangling bonds. Such dangling bond states might also be present on the measured part of the sample. This part of the sample lies outside the center, and was not heated to temperatures as high as in the center of the sample. Possibly graphene has not yet been formed on this part and only the buffer layer is present. As mentioned in the previous section, this buffer layer contains dangling bonds.

A peak is observed in all scattering geometries at 116meV. This peak is ascribed to and characteristic for a FK(Fuchs Kliewer surface phonon polariton) mode [63]. At momentum transfer close to the specular position a peak at 232mV is observed. This one is most

probably attributed to a double scattering contribution of the FK mode [63].

At the different scattering geometries the calculated momentum transfers covers a large part of the SiC Brillouin zone in the $\Gamma - K$ direction; the edge of which is situated at $k = 1.4\text{Å}^{-1}$. In this large range of momentum transfers no dispersion of the FK is observed.

The appearance of a Fuchs-Kliewer mode is expected [63] because SiC is an ionic compound. In compounds of which the crystal contains more than one ion specy, the different ions in the material typically have a different effective charge. This charge can cause an atomic displacement to effectively change a local dipole moment, creating the possibility of coupling to the electromagnetic field. Furthermore, atomic displacements near the surfaces can originate from either bulk phonon modes with non-zero displacement at the surface, or from a surface phonon mode which does not exist in the bulk. A Fuchs-Kliewer mode is a longitudinal charge density wave(polariton) due to the effective charge moved by a surface phonon.

Theoretically, using a semi-infinite dielectric half space model, does not predict a change of the FK-phonon frequency and only the first atomic layers at the surface can show a dispersion of the FK mode which is related to the mutual interaction of the electrical dipoles in the immediate surface layer. In our case the SiC(0001) surface is covered with one or more graphene layer and also the surface structure is different compared to the SiC(0001) surface and most or all of the Si-dangling saturated, which probably explains the lack of disperion Balster[34].

4.2.3 Measurements near the center

In figure 4.13 HREELS measurements taken at specular angle near the center of sample E are shown together with a specular measurement taken outside the center. The measurement near the center shows a much higher countrate of 33kcps compared to 5.1kcps for the measurement outside the center. The elastic peak is also much broader with a FWHM of 34mV compared to 23mV outside the center. The elastic peak shows a very long tail in comparison to the specular measurement taken outside the center. While outside the center the countrate at a loss energy of 75mv has already decreased to 1.6% of the elastic peak, the observed elastic peak near the center has only decreased to 10% of its maximum. The specular measurement also shows the FK-mode, with its maximum countrate located at 141mV, also showing a long tail similar to the elastic peak. In front of the onset of the FK peak, a small dip appears at 100mV.

The broadening can possibly be explained by a surface plasmon, as discussed in section 3.3.2 of [38]. This broadening is explained in relation to a broad surface plasmon contribution close to the elastic peak. This surface plasmon should be out of plane, eliminating the acoustical plasmon expected for free standing graphene as a candidate. Instead, due to the interaction between the substrate and the graphene layer, electrons are allowed to move in the direction perpendicular to the layer, allowing for a surface plasmon in this direction. Possibly in a mechanism similar to that described in [64].

Off specular measurements near the center, shown in figure 4.14 reveal the FK-mode and other peaks marked by vertical lines. First of all the FK-mode seems to lose intensity

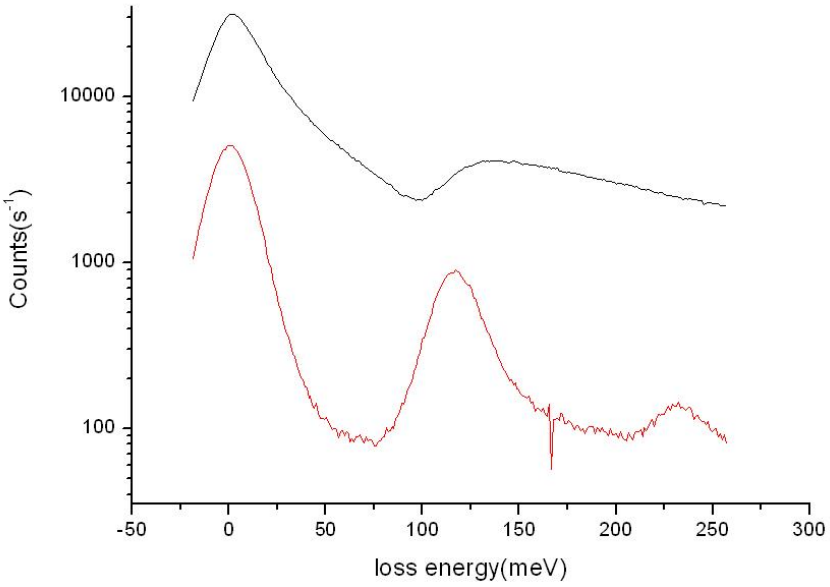

Figure 4.13: *Energy loss spectrum taken near the center of sample E(black line) compared with a spectrum taken outside the center(red line). Both spectra are taken at specular position.*

relative to the elastic peak as a function of momentum transfer until at $k \approx 0.5\text{Å}^{-1}$ it can no longer be distinguished.

At measurements with $k \geq 0.25\text{Å}^{-1}$, other peaks are observed, indicated in figure 4.14 with vertical lines. An overview of these peaks is shown in figure 4.15. As can be seen in this figure, the location of the observed peaks agree well with measurements done on graphite in the $\Gamma - K$ direction. However, not all the phonon branches show up in the HREELS measurements. Both acoustical and optical modes of the phonons with polarization in the longitudinal direction (denoted in figure 4.15 as LA and LO) and in the direction normal to the plane(denoted ZA and ZO) show peaks in the measurements at many different momentum transfers, but the shear horizontal optical(SHO) mode shows up in only one measurement, while the shear horizontal acoustical does not show up in any measurement. This can be explained by the selection rules of HREELS, as explained in [19].

In the previous section, it was established that possibly there is a monolayer of graphene present on the sample. However it could also be a bilayer of graphene. In this last case, it is expected that a phonon dispersion is found similar to that of graphite, since the interaction between the first and the second layer in graphene is expected to be very similar to graphite[31].

In case the sample contains a single layer of graphene, the situation is different. Single layers of epitaxial graphene can show a phonon dispersion which strongly deviated from that of graphite as showed in [3]. Since free standing graphene is expected to show the same phonon dispersion as graphite [35], such a difference in phonon dispersion can only be caused by interaction with the substrate. Such an interaction is also expected to alter the

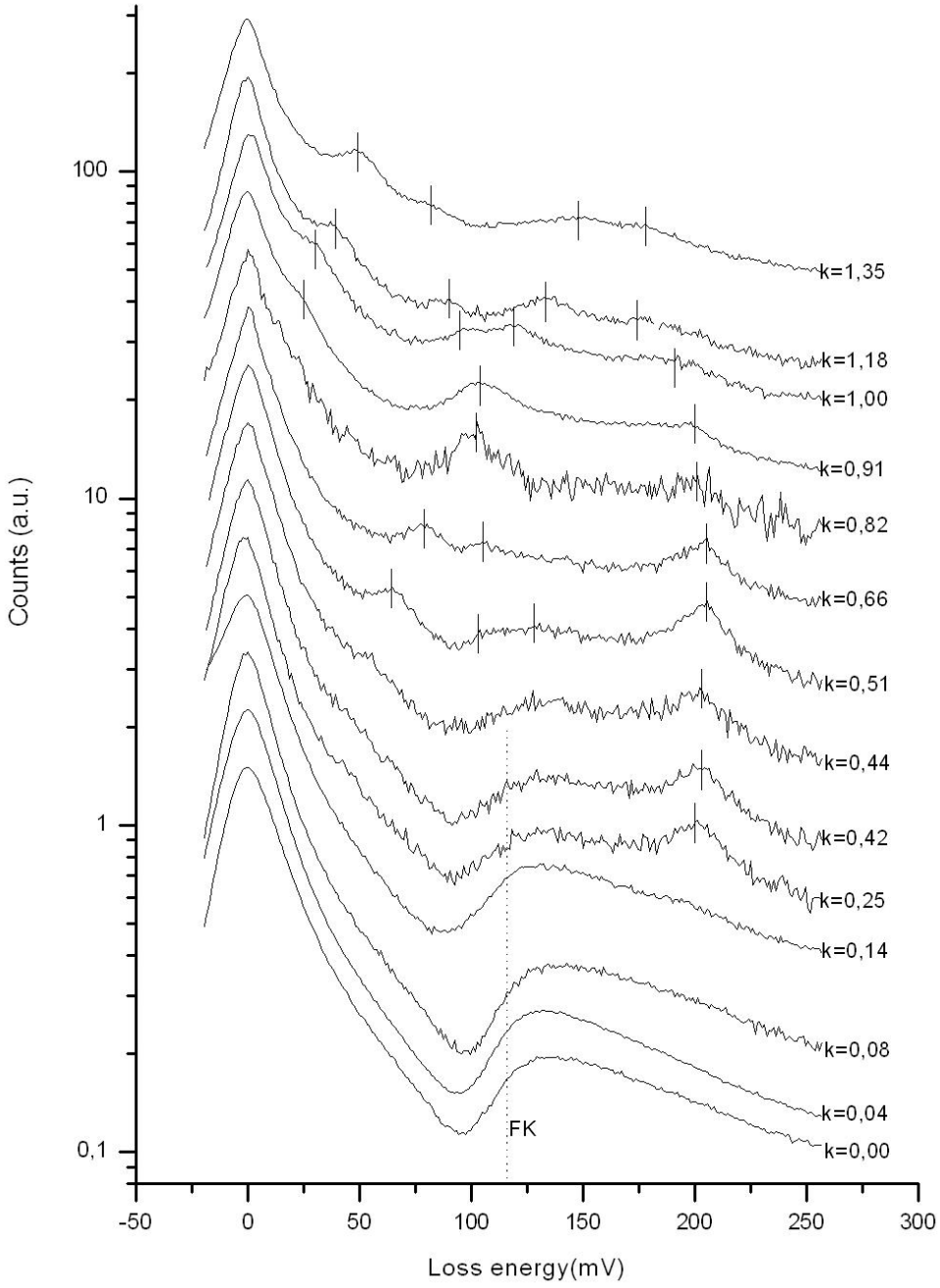

Figure 4.14: *Energy loss spectra taken near the center of sample E at different momentum transfer(denoted in* $\mathrm{\AA}^{-1}$*).*

band structure of the graphene. In [3], two monolayers on different surfaces are compared. A monolayer on a TiC(100) surface which shows the same phonon modes as graphite, and a monolayer on TaC(111) which shows a different phonon dispersion than graphite.

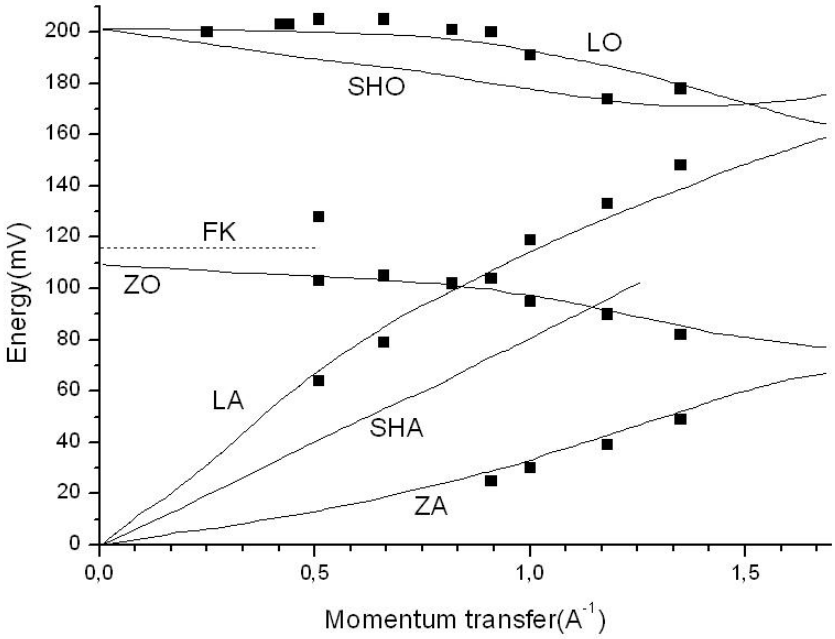

Figure 4.15: *An overview of the phonon modes determined in figure 4.14. The lines are drawn according to Siebenritt [33], where they connect the HREELS measurements done on graphite.*

The measured band structures, also shown in [3] for both these layers has been measured. The monolayer graphene on TaC(111) was found to show a band gap of 1.3eV and a doping resulting in a shift of the Dirac point of $E_D = -2$eV. While the monolayer of graphene on TiC(100) has much smaller doping, resulting in a shift of the Dirac point of $E_D = -0.5$eV. The band gap of graphene on TiC(100) has not been measured, possibly because it is larger than 0.5eV, in which case the top Dirac cone is above the Fermi energy and cannot be measured using photo emission experiments.

Of these two band structure measurements, the measurement of graphene on TaC seems to compare closely to measurements of graphene on SiC[39, 17]. Which explains why a phonon dispersion similar to graphite can be measured, in case of a single layer of graphene on top of SiC.

4.3 Conclusions

HREELS measurements done at the center and outside the center of the sample both reveal a Fuchs-Kliewer(FK) mode as is expected for SiC.

The measurement at the center of the sample reveals a phonon dispersion similar to that of graphite. This shows that either bilayer graphene has been formed on the sample, or a single layer with a weak interaction with the substrate.

Both at the center and outside the center, a broadening of the elastic peak is observed. Outside the center, which was heated to lower temperatures during its heat treatment,

a buffer layer is expected to be present account for the broadening on this part of the sample. Near the center an even larger broadening is observed which can be explained by the interaction between the graphene and the substrate.

4.4 General Conclusions

It is likely that one and two graphene layers have been grown on SiC(0001) with a ration of 4 to 1.

The measured DOS of both structures is slightly different and certainly for the first graphene layer, where the electronic states of the underlying buffer layer are measurable.

The phonon band structure is comparable to graphite and no phonon softening is obtained, which would indicate that the electronic interaction between the first graphene layer and the buffer layer is not very strong.

At this stage it is difficult to conclude whether or not the first graphene layer grown on SiC(0001) is comparable to a freestanding graphene layer.

Acknowledgements

I hereby show my gratitude for the opportunity of performing my master project at the Molecular Materials and Nanosystems Group. It has been a wonderful experience working not only with state of the art equipment, but most importantly, working with experienced people who have made the time to help me with the difficulties of doing research and writing my thesis.

I would like to thank my supervisor, Kees Flipse, who instead of dwelling on errors made, always looks for ways to improve the situation. I also enjoyed the directness in which he states his opinion. I would also like to thank Jiri Cervenka for the help and support he has given me. Of course this work also couldn't have been done without the help of many of the other group members, such as Gerard Wijers, our technician, who was always able to fix what I broke and Erwin Rossen, previously my fellow student and now PhD-student, who's structured approach has been a useful example.

Bibliography

[1] Wallace, P.R., The Band Theory of Graphite, Physical Review 71 (1947) 622

[2] Semenoff, G.W., Condensed-Matter Simulation of a Three-Dimensional Anomaly, Physical Review Letters, 53 (1984) 2449

[3] Oshima, C. *et al*, Ultra-thin epitaxial films of graphite and hexagonal boron nitride on solid surfaces, Journal of Physics: Condensed Matter 9 (1997) 1

[4] Geim, A.K. *et al*, Electric Field Effect in Atomically Thin Carbon Films, Science 306 (2004) 666

[5] Katsnelsen, M.I. *et al*, Chiral tunnelling and the Klein paradox in graphene, Materials Today 10 (2007) 20

[6] Zhang, Y. *et al*, Experimental observation of the quantum Hall effect and Berrys phase in graphene, Nature 438 (2005) 201

[7] Heersche, H.B. *et al*, Bipolar supercurrent in graphene, Nature 466 (2007) 56

[8] Uchoa, B. *et al*, Superconducting States of Pure and Doped Graphene, Physical Review Letters, 98 (2007) 146801

[9] McChesney, J.L. *et al*, Massive enhancement of electron-phonon coupling in doped graphene by an electronic singularity, arXiv:0705.3264v1

[10] Cheianov, V.V. *et al*, The focusing of Electron Flow and a Veselago Lens in Graphene p-n Junctions, Science 315(2007) 1252

[11] Tombros, N. *et al*, Electronic spin transport and spin precession in single graphene layers at room temperature, Nature 448 (2007) 571

[12] Rycerz, A. *et al*, Valley filter and valley valve in graphene, Nature Physics 3 (2007) 172

[13] de Heer, W.A. *et al*, Ultrathin Epitaxial Graphite: 2D Electron Gas Properties and a Route toward Graphene-based Nanoelectronics, Journal of Physical Chemistry B 108 (2004) 19912

[14] Peres, N.M.R. *et al*, Electronic properties of disordered two-dimensional carbon, Physical Review B 73 (2006) 125411

[15] Ramachandran, W. *et al*, Preparation fo Atomically Flat Surfaces on Silicon Carbide Using Hydrogen Etching, Journal of Electronics Materials 27 (1998) 308

[16] Persson,C. *et al*, Relativistic band structure calculation of cubic and hexagonal SiC polytypes, Journal of Applied Physics 82 (1997) 5496

[17] Bostwick, A. *et al*, Quasiparticle dynamics in graphene, Nature Physics 3 (2007) 36

[18] Pisana, S. *et al*, Breakdown of the adiabatic Born-Oppenheimer approximation in graphene, Nature Materials 6 (2007) 198

[19] Yanagisawa, H. *et al*, Analysis of phonons in graphene sheets by means of HREELS measurement and *ab initio* calculation, Surface and Interfaces Analysis 37 (2005) 133

[20] Rearick, D.J. *et al*, Design of a hydrogen etching system for surface preparation of SiC wafers, Journal of Vacium Science and Technology A 24 (2006) 1970

[21] Forbeaux, I. *et al*, Heteroepitaxial graphite on 6H-SiC(0001): Interface formation through conduction-band electronic structure, Physical Review B, 58 (1998) 16396

[22] Starke. *et al*, Morphology, bond saturation and reconstruction of hexagonal SiC surfaces, Applied Physics A 65 (1997) 587

[23] Mårtensson, P. *et al*, Atomic and Electronic structure of 6H-SiC surfaces, physics status soldi (b), 202 (1997) 501

[24] Charrier, A. *et al*, Solid-state decomposition of silicon carbide for growing ultra-thin heteroepitaxial graphite films, Journal of Applied Physics, 92 (2002) 2479

[25] Chen, W. *et al*, Atomic structure of the 6H-SiC(0001) nanomesh, Surface Science 596 (2005) 176

[26] Brar, V.W. *et al*, Scanning tunneling spectroscopy of inhomogeneous electronic structure in monolayer and bilayer graphne on SiC, arXiv:0706.3764

[27] Li, T., Characteristics of graphite films on silicon and carbon terminated faces of silicon carbide, PhD thesis(group of De Heer)

[28] Tsong, I.S.T. *et al*, Atomic structures of 6H-SiC(0001) and $(000\bar{1})$ surfaces, Surface Science 351 (1996) 141

[29] Kelly, F. *et al*, Nanoscale imaging of chemical interactions: Fluorine on graphite, Proceedings of the National Academy of Sciences 97 (2000) 10318

[30] Rollings, E. *et al*, Synthesis and charactarization of atomically thin graphite films on a silicon carbide substrate, Journal of Physics and Chisistry of Solids 67 (2006) 2172

[31] Varchon, F. *et al*, Electronic Structure of Epitaxial Graphene Layers on SiC:Effect of the Substrate, Physical Review Letters 99 (2007) 126805

[32] Seyller, Th. *et al*, Structural and electronic properties of graphite layers grown on SiC(0001), Surface Science 600 (2006) 3906-3911

[33] Siebenritt, S. *et al*, Surface phyonon dispersion in graphite and in a lathanum graphite intercalation compound, Physical Review B 55 (1997) 7927

[34] Balster, T. *et al*, Strong dispersion of the surface optical phonon silicon carbide in the near vicinity of the surface Brilloun zone center, Surface Science 600 (2006) 2886-2893

[35] Wirtz, L. *et al*, The phonon dispersion of graphite revisited, Solid State Communications 131 (2004) 141

[36] Castro Neto, A.H. *et al*, Substrate-induced bandgap opening in epitxial graphene, Nature Materials 6 (2007) 770

[37] Hwang, E.H. *et al*, Dielectric function, screening, and plasmon in two-dimensional graphite, Physical Review B, 75 (2007) 205418

[38] Ibach, H. *et al*, Electron Energy Loss Spectroscopy and Surface Vibrations, ISBN 0-12-369350-0

[39] Zhou, S.H. *et al*, Substrate-induced bandgap opening in epitaxial graphene, Nature Materials 6 (2007) 770

[40] Ohta, T. *et al*, Controlling the Electronic Structure of Bilayer Graphene, Science 313 (2006) 951

[41] Rutter, G.M. *et al*, Scattering and Interference in Epitaxial Graphene, Science 317 (2007) 219

[42] Melnichuk, A. *et al*, Effect of plasmon-phonon excitations on the coefficient of reflection from the surface of hexagonal silicon carbide, Journal of Experimental and Theoretical Physics, 89 (1999) 344

[43] Kelly, K.F. *et al*, Threefold Electron Scattering on Graphite Observed with C60-Adsorbed STM Tips, Science 273 (1996) 1371

[44] Mizes, H.A. *et al*, Long-Range Electronic Perturbations Caused by Defects Using Scanning Tunneling Microscopy, Science 244 (1989) 559

[45] Rutter, G.M. *et al*, Imaging the interface of epitaxial graphene with silicon carbide via scanning tunneling microscopy, arXiv:0711.2523v2

[46] Maultzsch, J. *et al*, Phonon dispersion in Graphite, Physical Review Letters 92 (2007) 075501

[47] Aizawa, T. *et al*, Bond softening in monolayer graphite formed on transition-metal carbide surfaces, Physical Review B, 42 (1990) 11469

[48] Emtsev, K.V. *et al*, Initial stages of the graphite-SiC(0001) interface formation studied by photoelectron spectroscopy, arXiv:cond-mat/0609383v1

[49] Persson, B.N.J. *et al*, Inelastic scattering of slow electrons from Si(111) surfaces, Physical Review B, 30 (1984) 5968

[50] G. Binnig, H. Rohrer, Ch. Gerber and E. Weibel, IBM J. Res. Dev. 30 (1986) 355

[51] K.W. Hipps, Scanning Tunneling Spectroscopy, Handbook of Applied Solid State Spectroscopy, ISBN: 978-0-387-32497-5

[52] R.J. Hamers, Ann. Rev. Phys. Chem. 40 (1989) 531-559

[53] Balster, T. *et al*, A study of surface band bendings and charge densities of SiC(001) 2×1 and c(2×2) by high-resolution electron-energy-loss spectroscopy, Surface Science 416 (1998) 177

[54] G. Ertl and J. Kppers, Low Energy Electrons and Surface Chemistry, VCH, Weinheim, 1985.

[55] N. R. Avery, Vibrational Spectroscopy of Molecules on Surfaces, Edited by J. T. Yates Jr and T. E. Madey, Plenum Press, New York, 1987, Chap. 6.

[56] D. M. Newns, Phys. Lett. 60A (1977) 461.

[57] A. Delanaye, A. A. Lucas and G. D. Mahan, Surf. Sci. 70 (1978) 629

[58] D. L. Mills, Surf. Sci. 48 (1975) 59

[59] M. A. van Hove, W. H. Weinberg and C. M. Chan, Low Energy Electron Diffraction, Springer Verlag, New York, 1986.

[60] E. A. Wood, J. Appl. Phys. 35 (1964) 1306.

[61] Van Bavel, A.P., Understanding and Quantifying Interactions between Adsorbates CO, NO and N- and O-atoms on Rh(100), PhD Thesis, ISBN 90-386-3026-3

[62] Rossen, E.T.R., Influence of substrate and tip on Inelastic Electron Tunneling Spectroscopy, Master Thesis at the group of M2N

[63] Nienhaus, H. *et al*, Phonons in 3C-, 4H-, and 6H-SiC, Surface Science 324 (1995) 328

[64] Kresin, V.Z. *et al*, Spectroscopy of the layered high-temperature superconductors and their collective plasmon modes - a model for phonon and plasmon-induced pairing, J. Opt. Soc. Am. B 6 (1989) 490

Old spectroscopy

Spectroscopy

Defects

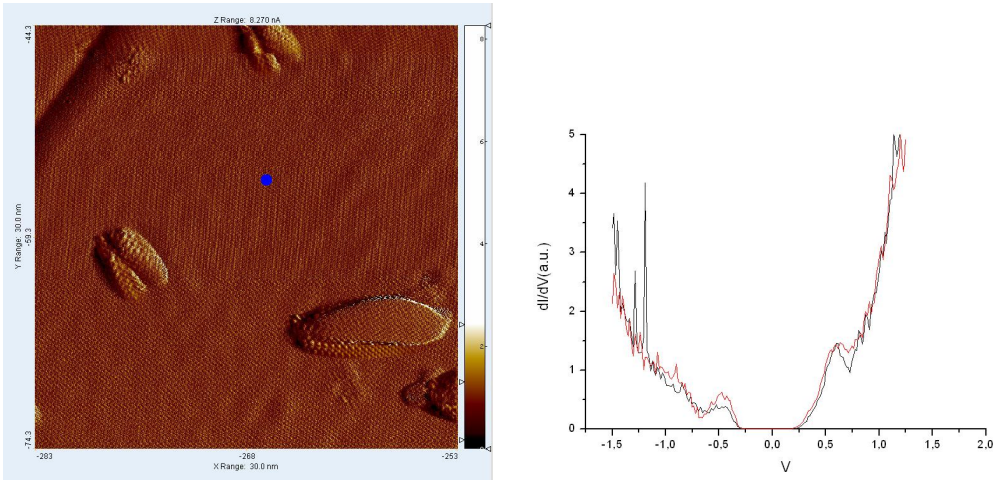

(a) **(b)**

Figure 16: *a) A* 30nm × 30nm *current image taken on sample C, at T=77K with* $V_{bias} = 0.90$V *and* $I_{setpoint} = 1.04$nA*, showing a blue dot indicating the position where spectroscopy has been performed. The position was chosen to be far away(*$\sim$ 8nm*) from defects which could have long range influence. b) Spectroscopy taken with lockin at* $V_{mod} = 12$mV*,* $f_{mod} = 1.8$kHz*, a lockin time constant of* 30ms *and a presample delay of* 270ms*.*

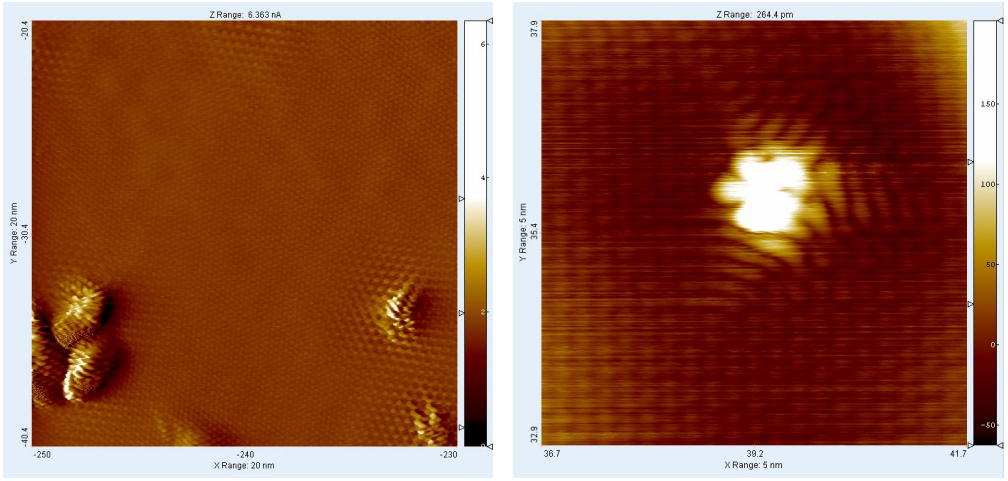

(a) **(b)**

Figure 17: *a) A* 20nm×20nm *current image taken on sample C, at T=77K with* $V_{bias} = -0.92$V *and* $I_{setpoint} = 1.70$nA*, showing a few defects, with a reconstruction, similar to the* $\sqrt{3} \times \sqrt{3}R30°$ *reconstruction around defects on graphite [29], reaching to* $\sim$ 5nm *away from the defects. b) A* 5nm × 5nm *current image taken on sample B, at T=77K with* $V_{bias} = -93$mV *and* $I_{setpoint} =$ 174pA*, showing a defect with a reconstruction similar to the prediction made for defects on graphite [29], spectroscopy of which is shown in figure 18.*

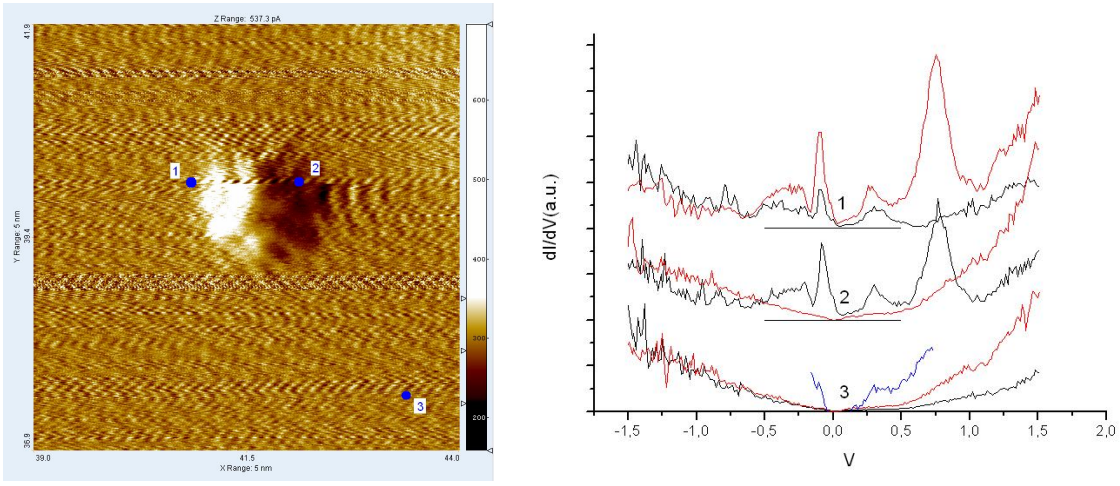

(a) **(b)**

Figure 18: *a) A* 5nm×5nm *Current image taken on sample B, at , at T=77K with* $V_{bias} = 1.50$V *and* $I_{setpoint} = 297$pA*, showing the defect also shown in figure* **??***, along with three measurements positions where spectroscopy has been measured. b) Spectroscopy taken with locking in both the forward direction(black) and the backward direction(red), at* $V_{mod} = 12$mV*,* $f_{mod} = 1.2$kHz*, a lockin time constant of* 10ms *and a presample delay of* 100ms*. The blue line shows a logplot of the spectroscopy taken at position 3 in the forward direction, showing a peak at* 0.3V*.*

Plasmons and dielectric function

The dielectric function in graphene is different from the dielectric function described in section **??**. First of all the linear band structure corresponds to zero effective mass. The plasmon frequency calculated in equation **??** diverges for effective mass going towards zero. So the presented simple model no longer applies.

Fortunately, much theory on the graphene dielectric function can be found. Moreover, two papers [37][**?**] seem to give very similar results for doped graphene, lending credibility to the difficult presented theory. The theory provides physical insight, and therefore a short summary of the theory will be given below.

The theory presented is the Random Phase Approximation(RPA). In this theory the dielectric function is written as[2]:

$$\epsilon(q,\omega) = 1 - v_c(q)\Pi(\mathbf{q},\omega) \tag{1}$$

, where $v_c(q) = \frac{2\pi e^2}{\kappa q}$ is the 2D coulomb interaction, with κ the dielectric constant of the substrate and $\Pi(\mathbf{q},\omega)$ is the dynamical screening equal to:

$$\Pi(q,\omega) = C\int d^2\mathbf{k} \sum_{B_1,B_2} f_{B_1,B_2}(\mathbf{k},\mathbf{k}+\mathbf{q})\frac{n_F(E_{B_1}(\mathbf{k})) - n_F(E_{B_2}(\mathbf{k}+\mathbf{q}))}{E_{B_1}(\mathbf{k}) - E_{B_2}(\mathbf{k}+\mathbf{q}) + i\eta} \tag{2}$$

where C is some constant, B_1 and B_2 are band indices, n_F is the Fermi-Dirac distribution function, η is an infinitesimal serving the mathematical purpose of keeping $\Pi(\mathbf{q},\omega)$ finite, and $f_{B_1,B_2}(\mathbf{k},\mathbf{k}+\mathbf{q})$ the band-overlap for graphene is given in both papers to be:

$$f(\mathbf{k},\mathbf{k}+\mathbf{q}) = \frac{1}{2}(1 \pm \cos\theta), \tag{3}$$

with θ the angle between $\mathbf{k}$ and $\mathbf{k}+\mathbf{q}$. The plus sign applies for an intraband transition, and the minus sign for an interband transition. $\Pi(\mathbf{q},\omega)$ is apparently a sum over all possible transitions from a filled electron state $\mathbf{k}$ to $\mathbf{k}+\mathbf{q}$ taking into account a certain cross-section represented by $f_{B_1,B_2}(\mathbf{k},\mathbf{k}+\mathbf{q})$ and $v_c(q) = \frac{2\pi e^2}{\kappa q}$ is a measure for how strongly such a transition couples to the electric field.

A possible transition is given in figure 19a. Notice that for every transition $\hbar|\omega| < \gamma q$, where γ is the linear relation between E and k as explained in section 2.1.2. Interband

[2]The related equation 2 of [37] seems to be erroneous, the correct equation is mentioned in the same paper just below the start of section III

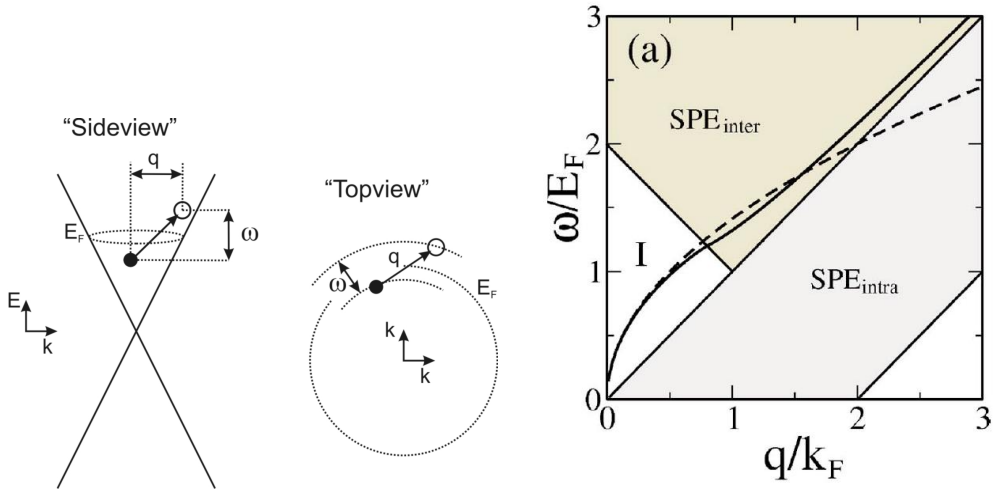

Figure 19: *a) Schematic representation of transition from a filled state to an empty state. b) Graph from [37] depicting the regions in the q, ω plane where single particle excitations can take place. The solid line shows the plasma dispersion, the dashed line shows the long wavelength limit of the plasma dispersion. $k_F = E_F/\gamma$.*

transitions require enough energy to go from beneath the Dirac energy, E_D, which is chosen to be zero, to above the Fermi energy E_F, thus requiring $\hbar\omega > E_F$, see figure 19b. Given that [17][36] $E_F \gtrapprox 400$mV, this falls outside the scope of the presented HREELS measurement, which go up to 250mV.

Calculations done [37] result in the following expression for the dielectric function in the long wavelength limit($q \to 0$):

$$\epsilon(q,\omega) \approx \begin{cases} 1 - \epsilon_b^{-1} \frac{E_F}{\gamma q}(1 + i\frac{\hbar\omega}{\gamma q}) & \hbar\omega < \gamma q \\ 1 - \epsilon_b^{-1} \frac{E_F \gamma q}{(\hbar\omega)^2}(1 - \frac{(\hbar\omega)^2}{4E_F^2}) & \gamma q < \hbar\omega < 2E_F \end{cases} \tag{4}$$

, where ϵ_b is the dielectric constant of the bulk, which is not very constant for SiC in the regime $\hbar\omega \approx 100$meV as will be shown in section**??**, however for simplicity ϵ_b will be taken to be constant. The difference between the exact plasmon dispersion and its long wavelength limit is small in the regime $\hbar\omega < E_F$ indicating that equation 4 is accurate in this regime.

LEED

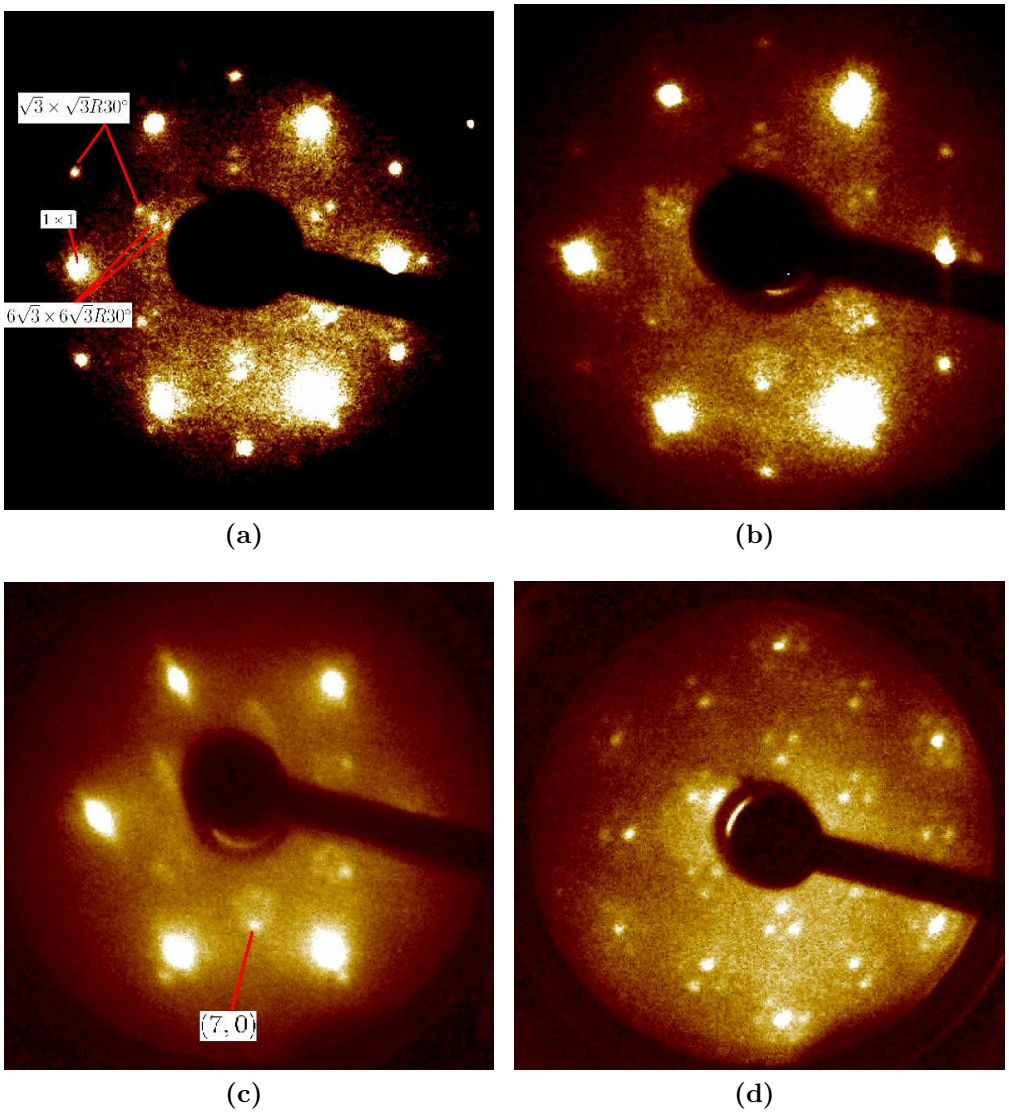

(a) **(b)**

(c) **(d)**

Figure 20: *a) LEED image at 100eV of sample E, after heating to* $1050°\mathrm{C}$ *for 10 minutes for the second time. b) LEED image at 100 eV after heating to* $1100°\mathrm{C}$ *for 3 minutes(second time). The* $6\sqrt{3}\times6\sqrt{3}R30°$ *seems more developed, for instance the* $(7,1)$ *spots are now visible.* $\sqrt{3}\times\sqrt{3}R30°$ *spots are also still visible. c) LEED image at 104 eV after heating to* $1150°\mathrm{C}$ *for 4 minutes. The* $6\sqrt{3}\times6\sqrt{3}R30°$ *looks very similar to the previous image, however,* $\sqrt{3}\times\sqrt{3}R30°$ *spots seem to have disappeared. d) LEED image at 98 eV after heating to* $1250°\mathrm{C}$ *for 4 minutes(with unknown overshoot). The* $6\sqrt{3}\times6\sqrt{3}R30°$ *(7,0) spot seems to have disappeared and graphitic* 1×1 *spots brighter than the SiC* 1×1 *spots seem to have appeared. Both the SiC and graphite* 1×1 *spots show* 6×6 *spots around them.*